DEVELOPMENT AND APPLICATION OF THREE-DIMENSIONAL IMPEDANCE MAPS RELATED TO TISSUE PATHOLOGY

BY

MICHAEL ROBERT KING

B.S., University of North Dakota, 2007

THESIS

Submitted in partial fulfillment of the requirements
for the degree of Master of Science in Electrical and Computer Engineering
in the Graduate College of the
University of Illinois at Urbana-Champaign, 2009

Urbana, Illinois

Adviser:

Professor William D. O'Brien, Jr.

ABSTRACT

Three-dimensional acoustic tissue models are a unique means to study ultrasonic scattering by tissue microstructure. In this work, the previous methods used to create and analyze these models were evaluated and refined. These techniques were then applied to a set of 10 human fibroadenomas, a benign tumor of the breast. These models, called three-dimensional impedance maps (3DZMs), are created from serial sets of histological images which must be properly transformed to recreate the original tissue volume. A properly reconstructed 3DZM can then be used to estimate properties, such as the effective scatterer size, of the ultrasonic scattering sites in the underlying tissue. These estimates can, in turn, be related to histological features of the tissue. For the fibroadenoma datasets, the average effective scatterer diameter was estimated to be 84 ± 40 μm when the entire volume was used for analysis. This result compared roughly to the size of the acini in the tissue, although a wide variation was observed in the histological layout of the tissue.

To Mom, Dad, Jake, and Gina

ACKNOWLEDGMENTS

I would like to sincerely thank several people for their support. I would like to thank my adviser, Dr. William D. O'Brien, Jr., for his guidance and patience. Also, I would like to acknowledge the contributions of Dr. Michael Oelze, and the contributions of those in the Bioacoustics Research Lab. I would also like to acknowledge the love, support, and guidance of my parents, Rob and Donna; my brother, Jake; and my beautiful fiancée, Gina. This work was supported by NIH CA111289.

TABLE OF CONTENTS

CHAPTER 1 INTRODUCTION 1

CHAPTER 2 THEORY 4

CHAPTER 3 IMPEDANCE MAP CONSTRUCTION 12

CHAPTER 4 IMPEDANCE MAP ANALYSIS 30

CHAPTER 5 DISCUSSION 53

REFERENCES 57

CHAPTER 1
INTRODUCTION

1.1 Overview

Medical ultrasound provides an inexpensive imaging modality when compared to other common modalities such as X-ray, computed tomography, or magnetic resonance imaging [1]. Additionally, ultrasound can be used for diagnostic medical applications without causing damage to tissue [2]. These advantages clearly motivate the development of additional diagnostic functionality in medical ultrasound.

While conventional ultrasound images provide only qualitative depictions of tissue macrostructure, quantitative ultrasound (QUS) seeks to provide quantitative information about tissue microstructure. This information could greatly improve the diagnostic functionality in medical ultrasound. However, this process depends on the use of appropriate models for ultrasonic scattering by tissue microstructure [3].

As a means to investigate ultrasonic scattering by tissue microstructure, a method was previously developed to create computational acoustic models of tissue microstructure [1]. These models, called three-dimensional impedance maps (3DZMs), provide a means to combine ultrasonic characterization of tissue with histological evaluation of the underlying tissue structure. This thesis investigates the development and analysis of these models, as well as their application to a common type of benign human breast tumor, the fibroadenoma. 3DZMs were made from a collection of human fibroadenoma samples, and were analyzed using the techniques described herein. These

results were then compared to the histological features of the tissue to identify possible scattering sources.

1.2 Quantitative Ultrasound

Conventional ultrasound images are derived from backscattered radio frequency (RF) echo signals. These echoes are a result of scattering by tissue macro- and microstructure with varying acoustic properties. Typically, the received RF signals are envelope-detected to produce an image, but this processing removes frequency-dependent information from the RF signal [4].

QUS uses the frequency information from the RF echo signal to deduce quantitative information related to the properties of the tissue microstructure. This frequency information can provide details about the statistical properties of the scattering structures, such as average size and average concentration. These additional parameters could serve to enhance the diagnostic capability of medical ultrasound. Parameterization of ultrasonic backscatter has been investigated previously as a means to extend the diagnostic capability of ultrasound [5],[6], and has demonstrated the ability to quantify ocular, liver, prostate, renal, and cardiac tissues [7]. To attain meaningful results, however, the relationship between backscattered frequency information and underlying tissue properties must be well understood.

1.3 Three-Dimensional Impedance Maps

3DZMs are volumes in which the value of each volume element (voxel) represents an acoustic impedance value. 3DZMs can be constructed from properly

aligned and reconstructed sets of histological images, or they can be simulated. The details of 3DZM construction are discussed in Chapter 3.

For media in which the variations in impedance are relatively small, this spatial impedance function can be related to the ultrasonic backscatter of the media by the spatial Fourier transform. This relationship is discussed in Chapter 2. In this way, 3DZMs can be used to study both the ultrasonic backscatter and the histological characteristics of a particular medium. This duality illustrates the utility of 3DZMs for the study of ultrasonic scattering in tissue as it relates to actual histological features of tissue microstructure; this concept is explored in Chapter 4.

CHAPTER 2

THEORY

2.1 Ultrasonic Scattering Theory

Ultrasonic scattering occurs when an incident pressure wave interacts with a volume with acoustic properties (compressibility κ and density ρ) that are different from those of the surrounding medium. Backscatter is the portion of this scattered sound that propagates in the opposite direction of the incident wave, which is of special interested for pulse-echo ultrasound [2]. This section reviews the theory of weak scattering [1], [6] as it is relevant to the study of scattering in tissue.

Weak scattering occurs when the acoustic properties of the scattering sites are very close to those of the surrounding medium. In this case, known as the *Born approximation*, it is assumed that the incident pressure wave remains essentially unchanged as it propagates through the scattering volume, and multiple scattering is ignored [2]. Consider a scattering volume V_0 with compressibility $\kappa(r)$ and density $\rho(r)$ in a medium with equilibrium compressibility κ_0 and density ρ_0. For a plane wave of unit amplitude with wave number k incident on the scattering volume, the backscattered pressure far from the volume ($r >> \lambda$) can be described by a spherical wave as

$$p_{bs}(r) = \frac{e^{-jkr}}{r}\Phi(2k) \tag{2.1}$$

where k is the acoustic wave number, r is the distance from the scattering site, and $\Phi(2k)$ is the angle distribution function. For weak scattering, this angle distribution function can be described as

$$\Phi(2k) = \frac{k^2}{4\pi} \iiint_{V_0} \gamma(r_0) e^{-2jkr_0} dV_0 \tag{2.2}$$

where

$$\gamma(r) = \gamma_\kappa(r) - \gamma_\rho(r) \tag{2.3}$$

with

$$\gamma_\kappa(r) = \frac{\kappa(r) - \kappa_0}{\kappa_0} \tag{2.4}$$

and

$$\gamma_\rho(r) = \frac{\rho(r) - \rho_0}{\rho(r)}. \tag{2.5}$$

The terms $\gamma_\kappa(r)$ and $\gamma_\rho(r)$ represent the relative change in compressibility and density at the scattering volume. For weak scattering, $\gamma_\kappa(r)$ and $\gamma_\rho(r)$ are small and $\gamma(r)$ can be approximated by a first-order Taylor series as

$$\gamma(r) = -2\frac{z(r) - z_0}{z_0} \tag{2.6}$$

where

$$z_0 = \rho_0 c_0 = \sqrt{\rho_0 / \kappa_0} \tag{2.7}$$

is the characteristic acoustic impedance of the background medium, and

$$z(r) = \rho(r)c(r) = \sqrt{\rho(r)/\kappa(r)} \tag{2.8}$$

is the acoustic impedance at the scattering volume. The sound speeds in the scattering volume and in the background medium are described by $c(r)$ and c_0, respectively.

Acoustic intensity, described by $I = P^2 / 2\rho_0 c$ for a spherical wave [8], where P is the peak pressure amplitude, can then be deduced for the backscattered wave as

$$I_{bs} = Ak^4 \left|\Phi(2k)\right|^2 \tag{2.9}$$

where A is some proportionality constant. By then substituting Equation (2.6) into Equation (2.2), the backscattered intensity for weak scattering can be expressed as

$$I_{bs} = A'k^4 S(2k) \tag{2.10}$$

where A' is a new proportionality constant and

$$S(2k) = \left| \iiint_{V_0} \frac{z(r) - z_0}{z_0} e^{-2jkr_0} dV_0 \right|^2 \tag{2.11}$$

is seen to be the squared modulus of the spatial Fourier transform of the relative impedance function, that is, the power spectrum of the relative impedance function [9]. The backscattered intensity divided by k^4 (or by frequency f^4 because $k = 2\pi f / c$) is then seen to also be proportional to the power spectrum of the relative impedance function. As will be seen later, this idea is instrumental in relating 3D impedance maps to ultrasonic backscatter.

2.2 Acoustic Form Factors

Acoustic form factors (FFs) are functions which describe the behavior of the backscattered intensity due to a single scattering volume as a function of frequency [10]. Form factors show the deviation in backscattered intensity for a particular scattering volume when compared to a Rayleigh scatter (which has only k^4 dependence). Regardless of the scattering volume geometry, the corresponding FF always approaches unity as k approaches zero, because the wavelength becomes very large and the scatterer appears as a point scatterer.

Form factors are related to the geometry of the scattering volume by the Fourier transform of the 3D spatial autocorrelation function of the volume, or equivalently by the squared magnitude of the 3D spatial Fourier transform of the volume (due to the Wiener-Khintchine theorem) [9]. Because of this, FFs are clearly proportional to the power spectrum $S(2k)$ of a scattering volume as described by Equation (2.11); equivalently, they are proportional to backscattered intensity when the k^4 dependence is removed.

If a scattering volume has spherical symmetry, then the corresponding FF function will only depend on the scatterer size, because the orientation of the volume is not important. In this case, scatterer size refers to either the average diameter for discrete scatterers or to the average correlation length for scatterers which are continuously varying functions [10].

The FF model used most frequently in this work is the fluid-filled sphere FF. This FF describes the acoustic scattering from a filled spherical volume of radius a and acoustic impedance z_s in a background of impedance z_0. This FF is expressed as

$$F_a^{fs}(2k) = \left(\frac{3 j_1(2ka)}{2ka} \right)^2 \tag{2.12}$$

where j_1 is the spherical Bessel function of the first kind and the superscript *fs* refers to fluid sphere. The FF is seen to be a function of frequency which depends only on the parameter a, the sphere radius. This is also known to be the 3D Fourier transform of a sphere [6]. Figure 2.1 shows a plot of the fluid-filled sphere FF as a function of frequency for several values of a. Figure 2.2 shows the same plot on a logarithmic scale.

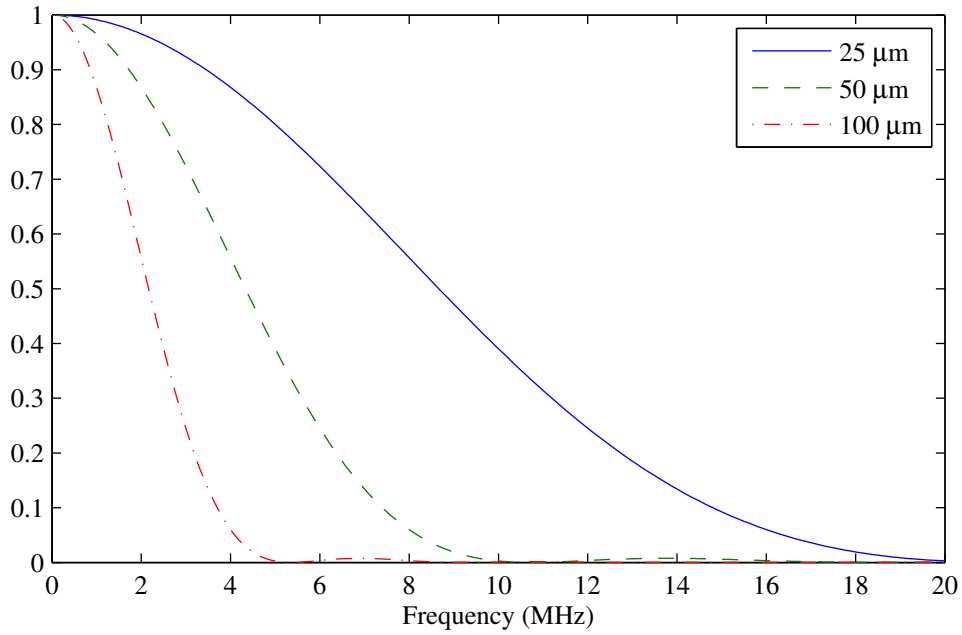

Figure 2.1 Fluid-filled form factor for a = 25, 50, and 100 µm.

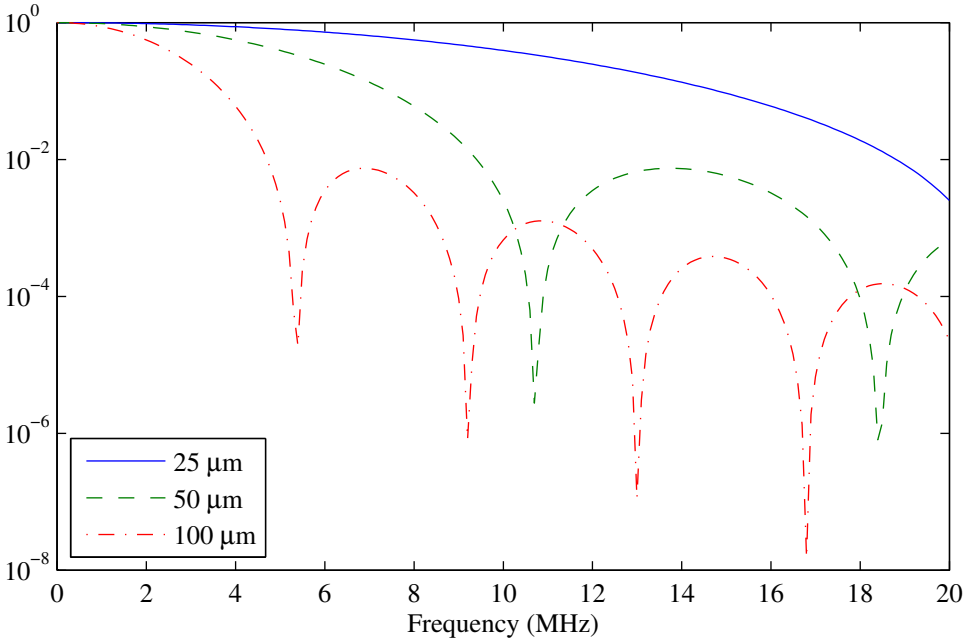

Figure 2.2 Fluid-filled form factor for a = 25, 50, and 100 µm, displayed on a logarithmic scale.

A second, commonly used FF model is the Gaussian FF. This FF describes the acoustic scattering from a volume which has acoustic properties which vary continuously

as a Gaussian function along any radial path away from the center of the volume. In this case, the FF is expressed as

$$F_a^g(2k) = e^{-0.827k^2a^2} \tag{2.13}$$

where, in this case, the superscript *g* refers to Gaussian.

2.3 Coherent and Incoherent Scattering

Acoustic FFs describe the behavior of the backscattered intensity due to a single scattering structure. Consider, then, a collection of identical, randomly positioned scattering structures with FF function $F_a(2k)$ and spatial relative impedance function $s_a(x)$. For simplicity, consider the 1D case, in which the scatterers are distributed randomly in only the *x* direction. Then, for a medium containing *N* non-overlapping scatterers, the impedance function can be described as

$$s_{ens}(x) = s_a(x - x_1) + s_a(x - x_2) + ... + s_a(x - x_N) \tag{2.14}$$

where $x_1, \ldots, x_N$ describe the random spatial delay of each scatterer, and the subscript *ens* refers to ensemble. Then, due to the linearity and shift properties of the Fourier transform [9], the spatial Fourier transform of $s_{ens}(x)$ can be expressed as

$$S_{ens}(k) = S_a(k)e^{-j2\pi kx_1} + S_a(k)e^{-j2\pi kx_2} + ... + S_a(k)e^{-j2\pi kx_N}\,. \tag{2.15}$$

Taking the squared magnitude of this quantity results in

$$\left|S_{ens}(k)\right|^2 = \left|S_a(k)\right|^2 \sum_{p=1}^{N} e^{-j2\pi kx_p} \sum_{q=1}^{N} e^{j2\pi kx_q}\,. \tag{2.16}$$

The product of summations can then be reduced by considering the symmetry present: for each pair *p* and *q* for which the exponential argument contains the term $p - q$, there is an opposite pair *q* and *p* for which the exponential argument contains the term $q - p$.

Application of Euler's identity allows this pair of exponentials to be rewritten as a cosine term. This is true for all $p \neq q$; for the N cases in which $p = q$, the exponential argument is zero and the exponential term evaluates to unity. Finally, by considering that $F_a(2k) = |S_a(k)|^2$ and letting $F_{ens}(2k) = |S_{ens}(k)|^2$, Equation (2.16) can be rewritten as

$$F_{ens}(2k) = F_a(2k)\left[N + 2\sum_{p>q=1}^{N} \cos(2\pi k(p-q)) \right]. \tag{2.17}$$

This equation describes the FF of the scattering ensemble. In this equation, the first term is referred to as the incoherent scattering term, as it does not relate to interaction between particles. Rather, it is simply the acoustic FF of the scattering volume, scaled by the number of scatterers N. The second term is referred to as the coherent scattering term, as the frequency of each cosine term depends on the relative position of the scatterers within the volume. For a large number of randomly positioned scatterers and for $k > 0$, this term presents itself as random variation about the scaled FF of the scattering volume with an expected value of zero [11]. Figure 2.3 shows an example of the FF computed from a scattering ensemble containing identical, randomly positioned scatterers. The FF from a single scattering volume is also shown for comparison. In this example, the variations about the FF for a single scattering volume caused by the coherent scattering term can be seen. As expected, this effect is much more pronounced at lower frequencies. Figure 2.4 shows a rendering of the scattering volume used to generate Figure 2.3.

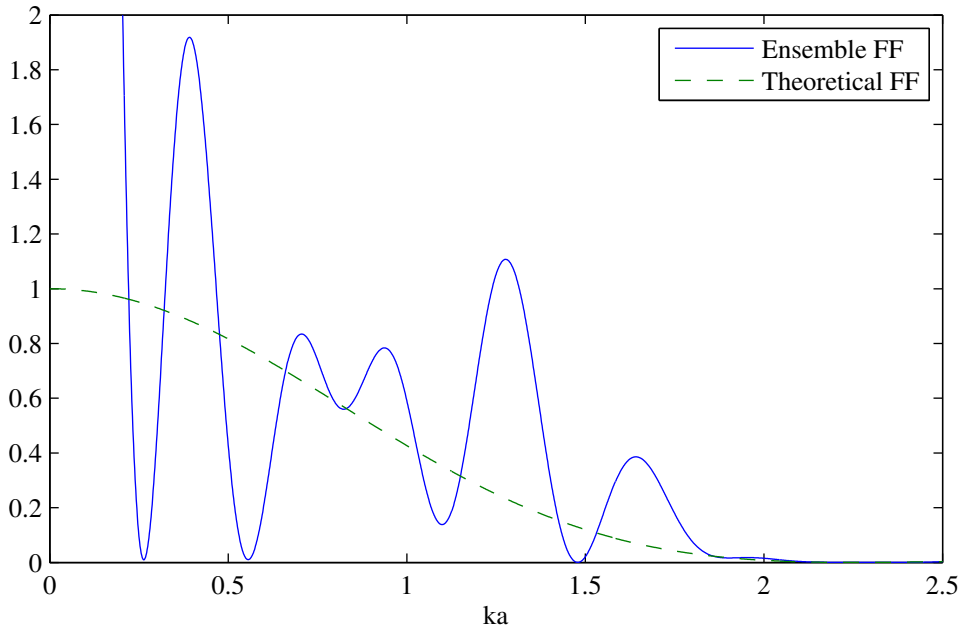

Figure 2.3 Form factor of a scatterer ensemble compared to the form factor for a single scatterer. The ensemble was composed of 26 randomly positioned, spherical scatterers with a = 8 μm.

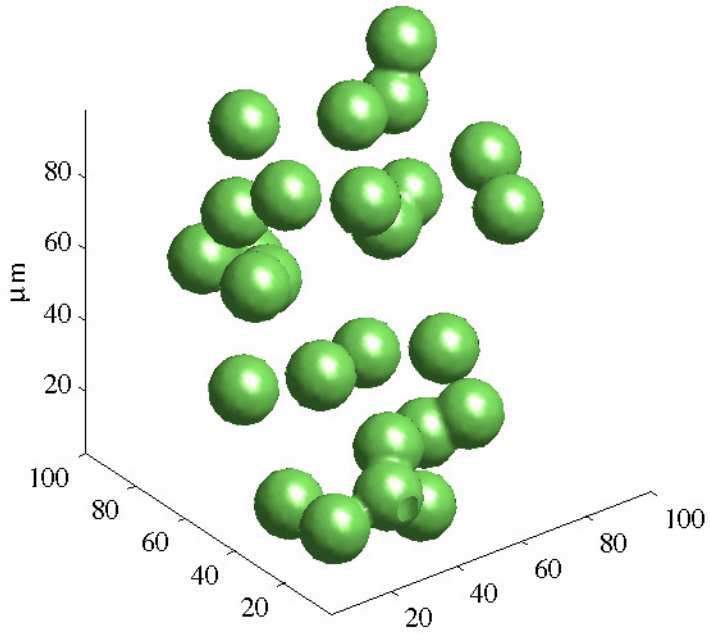

Figure 2.4 3D rendering of a scattering ensemble.

CHAPTER 3
IMPEDANCE MAP CONSTRUCTION

A three-dimensional impedance map is a computational phantom of which each element represents an estimate of the acoustic impedance value of the underlying medium. A technique for the creation of 3DZMs has been developed previously by Mamou [1]. This chapter provides a brief summary of this technique, followed by a description of the updates and modifications that have been made to this process. Finally, several examples of 3DZMs created from human breast tumors are presented.

3.1 Three-Dimensional Impedance Map Creation Overview

The 3DZM creation process begins with a set of photomicrographs (optical images taken at high magnification) of a tissue sample which has been fixed in formalin, embedded in paraffin, sectioned, placed on glass slides, and stained with hematoxylin and eosin (H&E). In order that this set of 2D images be converted into a 3D volume, several effects of the preparation process must be undone. An overview of this creation process is depicted in Figure 3.1.

First, the images need to be properly registered to each adjacent section so that the position within the original volume is properly restored. In addition to simple translational and rotational (that is, rigid) registration, the sections must be adjusted for any stretching or shearing that occurred as a result of the tissue slicing. Second, the photometric properties of the tissue must be equalized. Slight variation in the thickness of each section results in varying uptake of the H&E stain; the image properties must be

equalized to account for this. Third, some sections are inadvertently destroyed during the sectioning process, so these missing sections must be filled in to complete the reconstruction of the tissue volume. Finally, each element of the tissue volume must be assigned an acoustic impedance value. This is done based on the color value of the pixel, because the H&E staining causes tissue with a greater protein concentration to appear pink and tissue with a greater nucleic acid concentration to appear blue.

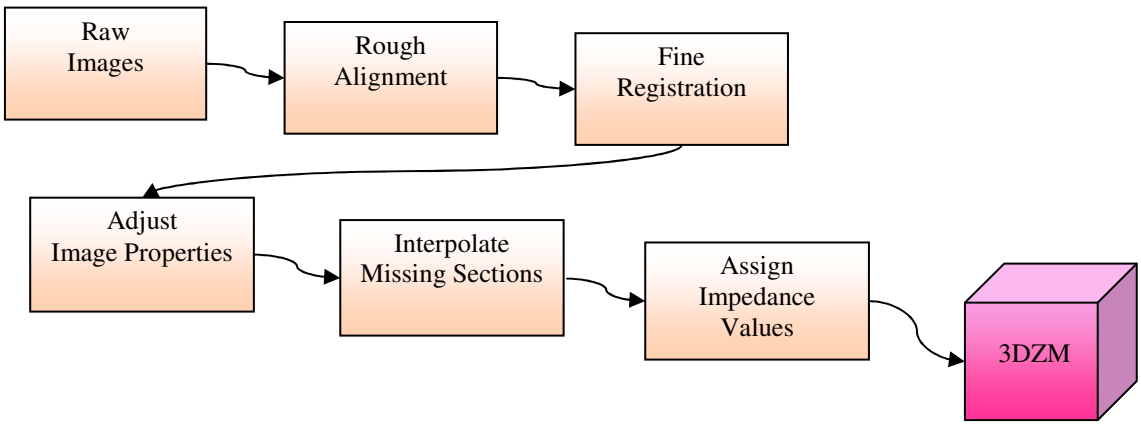

Figure 3.1 Overview of the 3DZM creation process.

3.1.1 Image registration

The image registration step in the 3DZM creation process seeks an optimal set of six transformations (horizontal and vertical translation, rotation, horizontal and vertical scaling, and shear) which align each image to the previous image in the set. Optimality is defined by the minimization of some similarity metric; in this case, normalized mutual information (NMI) was selected as the metric due to its robustness [1]. Thus, the algorithm seeks to maximize NMI, or equivalently to minimize the negative NMI.

The registration of two sections begins by testing a series of random rigid registration values to locate a good staring location which best maximizes the NMI. Next, a Nelder-Mead simplex search [12] is performed, beginning at this starting location. First,

only the rigid parameters are optimized in this way; the result of this search is then used as the initial condition for another simplex search in which all six affine parameters are optimized, producing the final transformation values.

3.1.2 Photometric equalization

The original 3DZM creation technique applied image contrast adjustment [13] to each image as a means to correct for photometric discrepancies. This technique transforms the image intensity values in such a way that the image histogram is made to better approximate a uniform distribution. This transformation was applied separately to each color component (that is, red, green, and blue or RGB). However, this approach tends to alter the color values of the image [13]. Because the impedance assignment step in the creation process depends upon the specific color values of the image, this step was modified to prevent the alteration of the image color values; this modification is described later in Section 3.5.

3.1.3 Missing section interpolation

Following the registration and photometric adjustment steps, the computed transformations are applied to each image and a volume is assembled. However, at this stage several sections may still be missing. These missing sections are replaced by interpolated sections by using cubic Hermite interpolation along each stacked column of pixels [1].

3.2 Image Acquisition

The 3DZMs presented in this thesis were all generated from images acquired using the NanoZoomer HT slide scanner (Hamamatsu, Hamamatsu City, Japan). The system was set to acquire images with a pixel resolution of 0.46 μm per pixel, and each section was sliced to a thickness of approximately 3 μm.

The NanoZoomer automatically locates a tissue section on a slide and scans only the selected region; this generally results in an image of a section with side length on the order of 1 cm. Computationally, this is much too large for direct use (the images are frequently up to 6 GB in size), but it enables the creation of multiple 3DZMs from a single dataset.

3.3 Global Section Alignment

The tissue sections in the raw image sets from the NanoZoomer are not rigidly aligned. In fact, the images do not necessarily have the same dimensions. This introduces a global alignment step into the 3DZM creation process. Initially, this was addressed by the creation and use of a manual section alignment program. Later, the process was automated. Regardless of which method is employed, a good global alignment of each section makes the succeeding registration steps much easier and more robust.

3.3.1 Manual global section aligner

Manual section alignment is accomplished using a graphical user interface (GUI) written for MATLAB (The Mathworks, Natick, Massachusetts) called *NZalign*. This program displays two semi-transparent sections and allows the user to translate and rotate

one of the sections until the alignment is satisfactory. The transformations needed to align each section are then saved, to be used later in the 3DZM creation process.

3.3.2 Automatic global section aligner

Automatic global section alignment is performed on a highly downsampled, grayscale version of the original tissue image. For each pair of images to be aligned, the first image is resized such that the number of rows is reduced to 100 and the number of columns is reduced accordingly so that the image aspect ratio is properly maintained. The second image of the pair is then downsampled by the same factor as the first; both are interpolated using bicubic interpolation. Raw images from the NanoZoomer may have more than 30 000 pixels per side, so this represents a downsampling factor of about 300. This downsampling is done to reduce the amount of computation needed. The alignment of these downsampled images provides a coarse initial registration which is refined later in the 3DZM creation process.

For each pair of tissue section images, alignment is performed in a series of steps. First, only translation is optimized by performing a dense search to minimize the pixelwise mean-squared error (MSE) between the images. This effectively places the two tissue sections roughly on top of each other. Next, a rough rotational and translational optimization is performed. Rotation values are applied at five-degree intervals, a local MSE based translational optimization is performed at each interval, and the pixelwise correlation coefficient [13] is maximized. The correlation coefficient between images x and y is defined as

$$corr(x, y) = \frac{E[(x - \mu_x)(y - \mu_y)]}{\sigma_x \sigma_y} \tag{3.1}$$

where μ_x and σ_x represent the mean and standard deviation, respectively, of image x; likewise for μ_y, σ_y, and image y. Finally, beginning at the translation and rotation values determined earlier, a simplex optimization is performed on the translational and rotational transformations to maximize the correlation coefficient between the images to attain the final set of transformations, which are then saved for later use.

For this automated alignment, the correlation coefficient was selected as a similarity metric to exploit the statistical similarity between each image pair. Both MSE and the image correlation coefficient were tested. The correlation coefficient was seen to be a much more reliable and robust similarity metric. The computational complexity of the correlation coefficient is also greater than MSE, but for this work, the quality and robustness of the alignment superceded the computational speed.

3.4 Neighborhood Subimage Alignment

The images acquired from the NanoZoomer are very large, so only a small subimage is used for the creation of a 3DZM. Because of this, a much larger region surrounding the each subimage may be extracted and used for image registration, allowing for translational alignment errors during the global section alignment step.

This step assumes that the global alignment transformations have located a correct rotation value, hence this search is only done to correct for errors in translation. The rationale behind this assumption is that the global alignment step is performed on a highly downsampled image pair, for which the rotational transformation will still be the same as for the full images. However, in this same case, a translational error of a single

pixel would correspond to a translational error of 300 pixels for a downsampling factor of 300.

As with the global alignment, the neighborhood search is performed using downsampled images. In this case, the images are downsampled by a factor of about 10. Again, this affords a reduction in computation while increasing the robustness of the 3DZM creation process by improving the initial conditions for later registration steps.

The neighborhood search is conducted for a pair of images with the first image having dimensions equal to seven times those of the original subimage and the second image having dimensions equal to three times those of the original subimage. The second image is translated across the larger, first image over a dense set of points, and the translation values which maximize the correlation coefficient are saved for use later in the 3DZM creation process.

3.5 Photometric Adjustment

By using the NanoZoomer for image acquisition, it can be assumed that the lighting conditions and properties of the imaging system are identical for all images within a set. However, some variation in the overall brightness of each image still exists due to variations in the thickness of the tissue slice and variations in the staining time. The notion of *saturation* refers to the dilution of a pure color by whiteness [13]; an unsaturated color appears white, while a highly saturated color appears as a pure color. Then, for stained tissue images, it can be argued that a section which has absorbed more stain will be more highly saturated in comparison to a section which has absorbed less stain. In order to correct for this effect, the image saturation was modified according to

$$S_{adj} = (S - \mu_S)(\frac{\sigma_{S,vol}}{\sigma_S}) + \mu_{S,vol} \tag{3.2}$$

where S is the original image saturation, S_{adj} is the adjusted image saturation, μ_S and σ_S are the image saturation mean and standard deviation, respectively, and $\mu_{S,vol}$ and $\sigma_{S,vol}$ are, respectively, the saturation mean and standard deviation for the entire volume. This transformation normalizes the mean and standard deviation of the saturation of each image within the volume to that of the overall volume, thus adjusting for varying levels of stain uptake. The advantage of this routine is that the original color information in the image is preserved. For display purposes, a similar transformation was applied to the intensity (grayscale) component of each image. However, because these components do not carry any color information, this is not a necessary step in the 3DZM creation process.

As an example of this saturation adjustment, two tissue sections are shown in Figure 3.2. These sections can be seen to have a difference in brightness levels. Figure 3.3 shows the histogram of the saturation components of these images. Clearly, the saturation values in each image are seen to fall within different ranges.

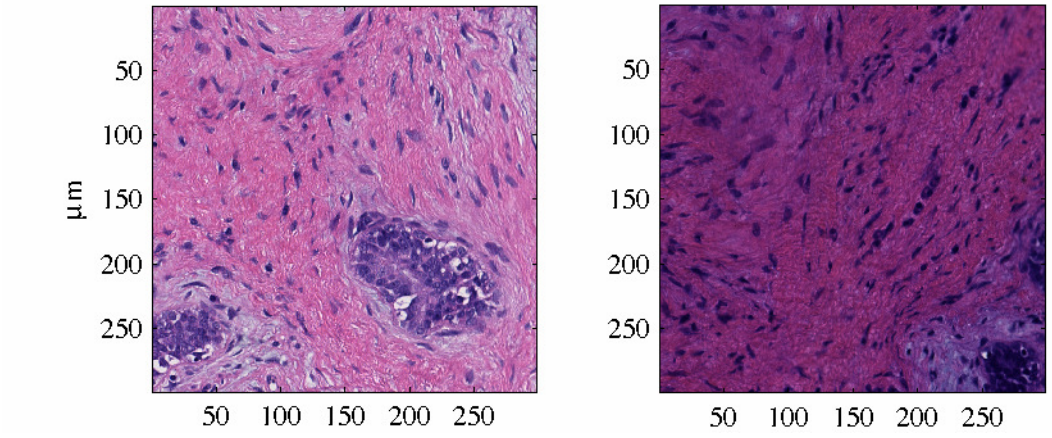

Figure 3.2 Original tissue section images. The image on the right is seen to have a lower overall brightness level compared to the image on the left.

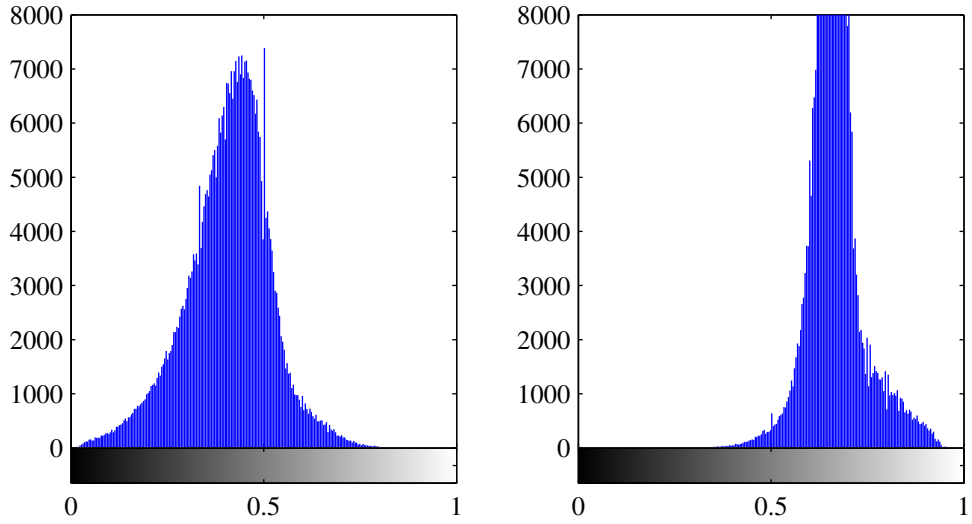

Figure 3.3 Original saturation value histograms corresponding to the images in Figure 3.2.

While saturation indicates the dilution of a pure color by whiteness, the notion of *hue* refers to the pure color itself. The histograms of the hue components of each image are shown in Figure 3.4. It is seen that the hue components of each image fall within the same range of hue values, motivating the adjustment of only the saturation components.

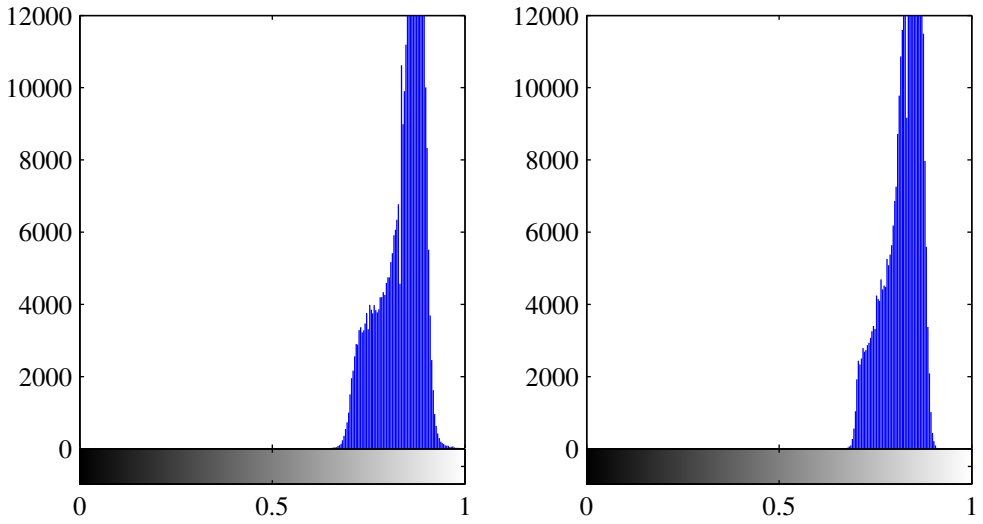

Figure 3.4 Original hue value histograms corresponding to the images in Figure 3.2.

The saturation adjustment described by Equation (3.2) equalizes the mean and standard deviation of the image saturation values, as illustrated in Figure 3.5. In the figure, the histogram of the second image is seen to be shifted and slightly stretched so that the saturation values of each image fall within roughly the same range. Figure 3.6 shows the resulting image pair after this adjustment has been applied.

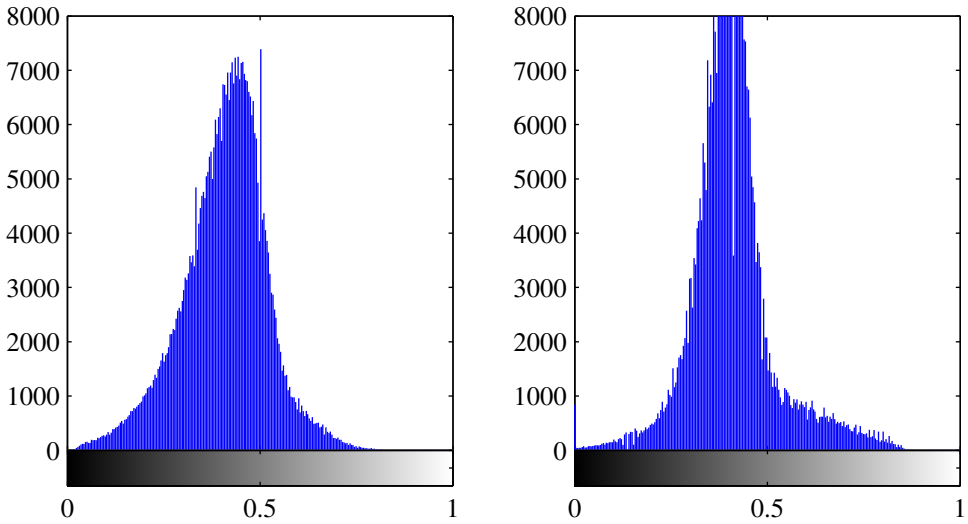

Figure 3.5 Adjusted saturation value histograms corresponding to the images in Figure 3.2.

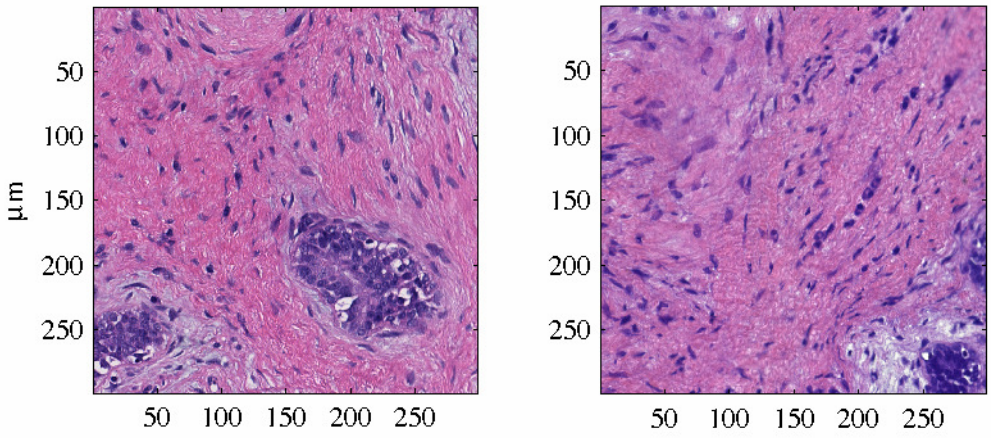

Figure 3.6 Tissue section images after saturation adjustment has been applied. The brightness levels of the images are now roughly the same.

3.6 Impedance Assignment

As discussed previously, impedance assignment is performed based on color thresholding of the stained tissue images. The staining of the tissue was used to differentiate the underlying tissue components. Impedance values were assigned by associating particular impedance values with certain color ranges, using values appropriate for each tissue structure.

3.6.1 HSI color space

The Hue-Saturation-Intensity (HSI) color space is well suited for converting the color images into impedance images. This is because the HSI color space represents colors in a way similar to the human descriptions of these colors. Hue describes the pure color (i.e., red, yellow, purple, etc.), while saturation describes the degree to which the color is diluted by whiteness. Intensity describes the gray level of the image, and does not carry color information [13].

The HSI color space is therefore very useful when a quantitative differentiation of, for example, *light pink* and *dark pink* is desired. The assignment of impedance values is done based on this very principle.

3.6.2 Impedance value selection

The assignment of impedance values is a critical step in the 3DZM creation process. It is also a very challenging step, as the acoustic impedance of the individual constituents of tissue may be estimated, but are difficult to directly measure. Thus, in a manner consistent with previous 3DZM work [1], impedance values were assigned based

on reasonable estimates which related stained tissue color to particular elements of tissue microstructure. Then, the acoustic properties of these elements could be estimated and related to the color of the stained tissue image.

Tissue areas with eosin staining (indicating protein concentration) range in color from light pink to dark pink, while tissue areas with hematoxylin staining (indicating nucleic acid concentration) range in color from light blue to dark blue. For this work, it was assumed that the pink image elements represented cell cytoplasm, while the blue image elements represented cell nuclei. Other image elements which appeared very light or white were assumed to be fat. Thus, impedance values were assigned based on image color as indicated in Table 3.1.

Table 3.1 Impedance assignment values.

Color	**Tissue component**	**Impedance value range (Mrayls)**
Light to dark pink	Cytoplasm	1.5 – 1.7
Light to dark blue	Cell nuclei	1.8 – 2.0
White	Fat	1.45

3.6.3 Image color thresholding

Impedance value assignment was accomplished by color thresholding. This was done in two steps. The first step involved the thresholding of the image hue, thereby categorizing each image element as either pink or blue. The second step involved the thresholding of the image saturation, further categorizing each element as white, light, or dark. Thus, each element was placed into a single hue-saturation category which could be directly mapped to an impedance value.

The saturation thresholding step also allowed the introduction of additional impedance levels by subdividing the range between light and dark. Throughout this work,

three subdivisions were used. Then, for example, the range of impedance values corresponding to pink hues was divided into three bins: 1.5 Mrayls for light pink, 1.6 Mrayls for medium pink, and 1.7 Mrayls for dark pink. Typical saturation values for the tissue images fell between 0.0 and about 0.8. Thus, the subdivision of the saturation values was applied within this range, and pixels with a saturation value greater than 0.8 were lumped into the highest category.

A test was run to investigate the effects of subdividing the impedance ranges. In this test, a registered histological map was color thresholded as described, while the number of subdivisions in each impedance range was varied from 1 to 20. The spatial power spectrum of the resulting 3DZM was then estimated (Section 4.1). Comparison of these power spectra was used as a means to observe the effect of the number of impedance subdivisions. Figure 3.7 shows the mean squared error (MSE) of the power spectrum at each subdivision level when compared to the power spectrum for the preceding subdivision level. These MSE values are normalized to a maximum of unity.

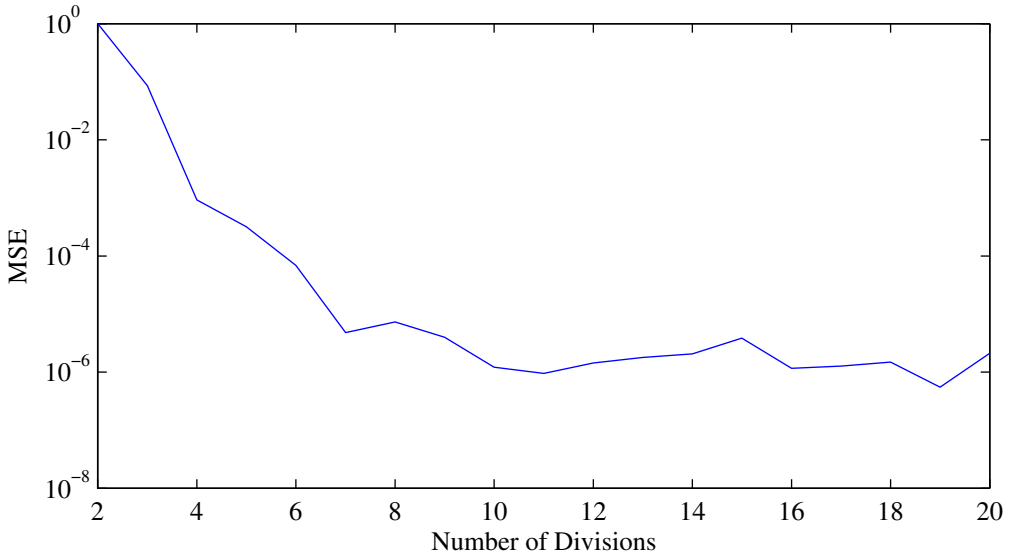

Figure 3.7 MSE of power spectra at each subdivision level when compared to the power spectrum at the previous subdivision level.

Clearly, additional impedance value subdivisions cause decreasing change between subsequent power spectra. Figure 3.8 shows the first three power spectra, for two, three, and four subdivisions. It can be seen that the power spectra for three and four subdivisions are nearly indistinguishable.

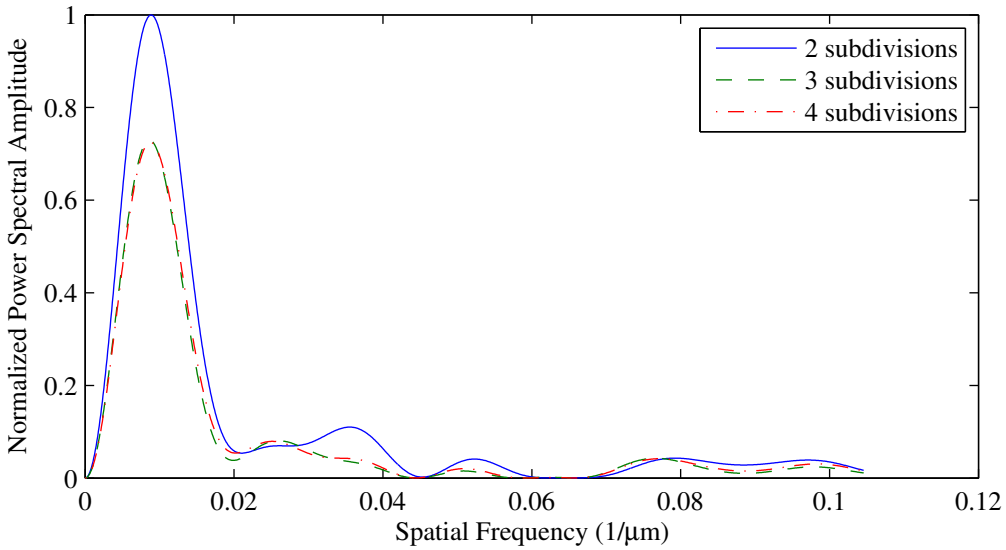

Figure 3.8 Power spectra for 2, 3, and 4 subdivisions of the impedance ranges.

Three subdivisions were chosen for this work because, as the example in Figure 3.7 suggests, the spectral change between two and three subdivisions was substantial, while the spectral change between three and four subdivisions was almost a factor of 100 smaller. The choice of three subdivisions capitalized on this, while still maintaining a fairly simple model. When scatterer size estimates were made from these power spectra (Sections 4.2), the results were identical for three or more subdivisions.

3.7 Three-Dimensional Impedance Map Creation Results

3DZMs were made from a collection of human fibroadenoma (a benign tumor of the breast) samples using these techniques. A sample of the resulting three-dimensional histological maps (3DHM) and 3DZMs are presented here.

Figure 3.9 shows a 3D rendering of a 3DHM created from a fibroadenoma dataset called WI #53. This rendering was created using MATLAB. The top face of the cube shows an image from the set, while the two visible side faces show images which were synthesized as a result of the image alignment and restoration.

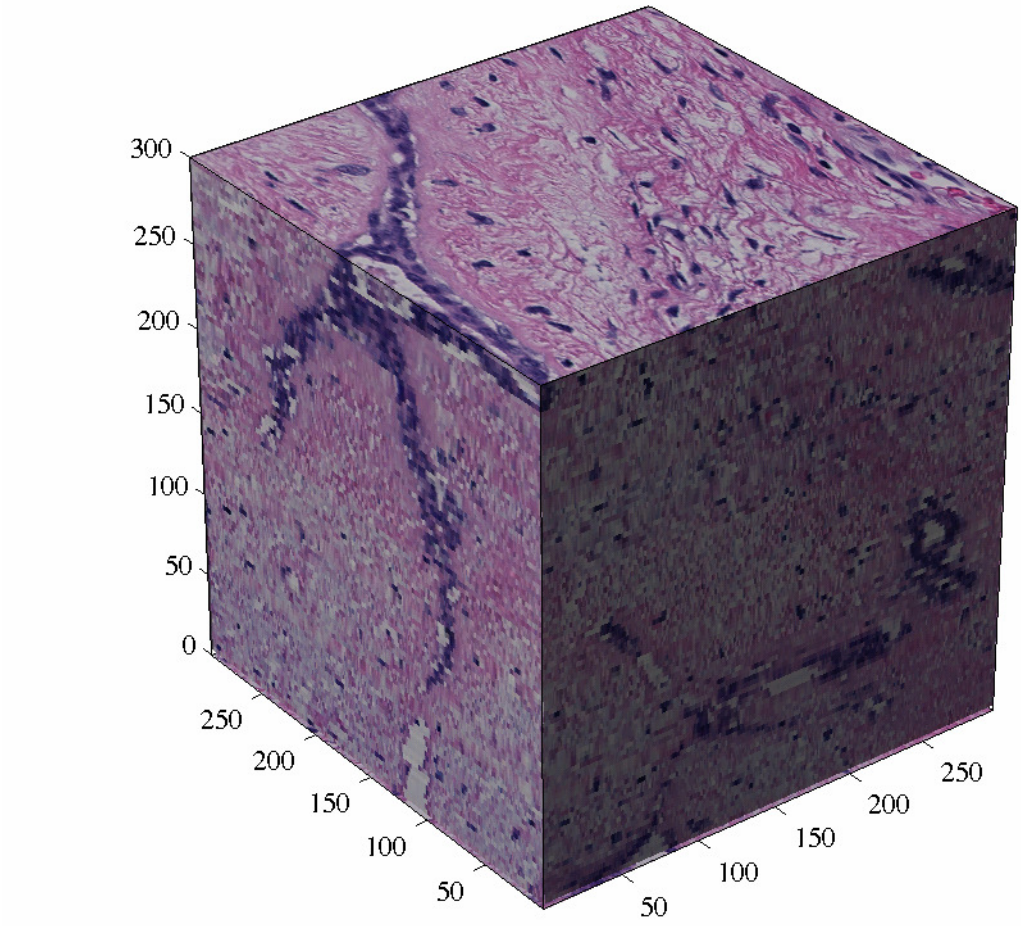

Figure 3.9 3D rendering of WI #53 3DHM.

Two slices from this 3DHM are shown in Figure 3.10. The first image was created by making a vertical cut through the volume, while the second image is an original image from the dataset, that is, a horizontal slice through the volume. From this figure, it can be seen that the reconstructed image has similar features to the image from the original dataset. Visually, this suggests that the reconstruction process has attained some level of success, although it does not provide any quantitative measure. It should be noted that the first image appears to be blurred when compared to the second image; this is because the slice thickness of 3 μm provides much coarser sampling than the image pixel resolution of 0.46 μm.

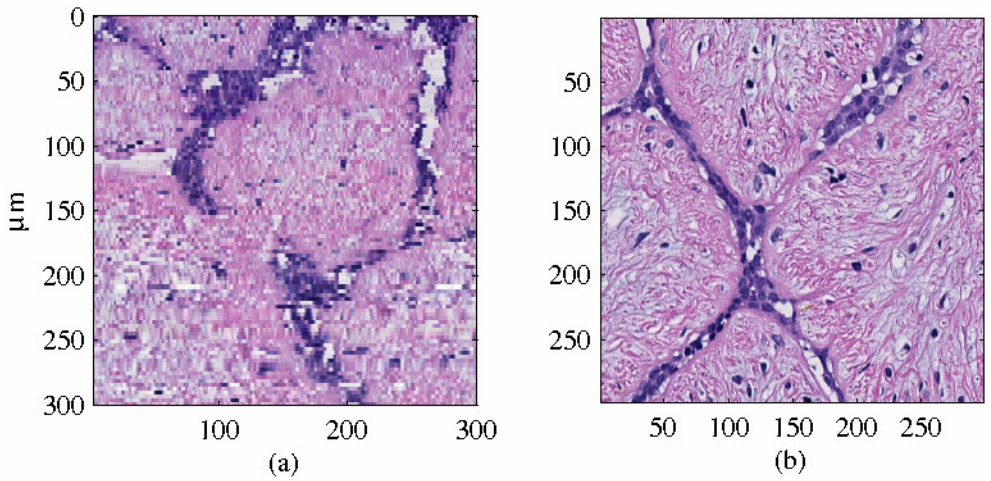

Figure 3.10 Histological sections from WI #53. Image (a) is a vertical slice through the volume; image (b) is an original image from the set.

Finally, Figure 3.11 shows a rendering of the WI #53 volume after impedance values have been assigned. This volume is depicted as a pseudo-color image, where each impedance value is assigned a particular intensity level for display purposes.

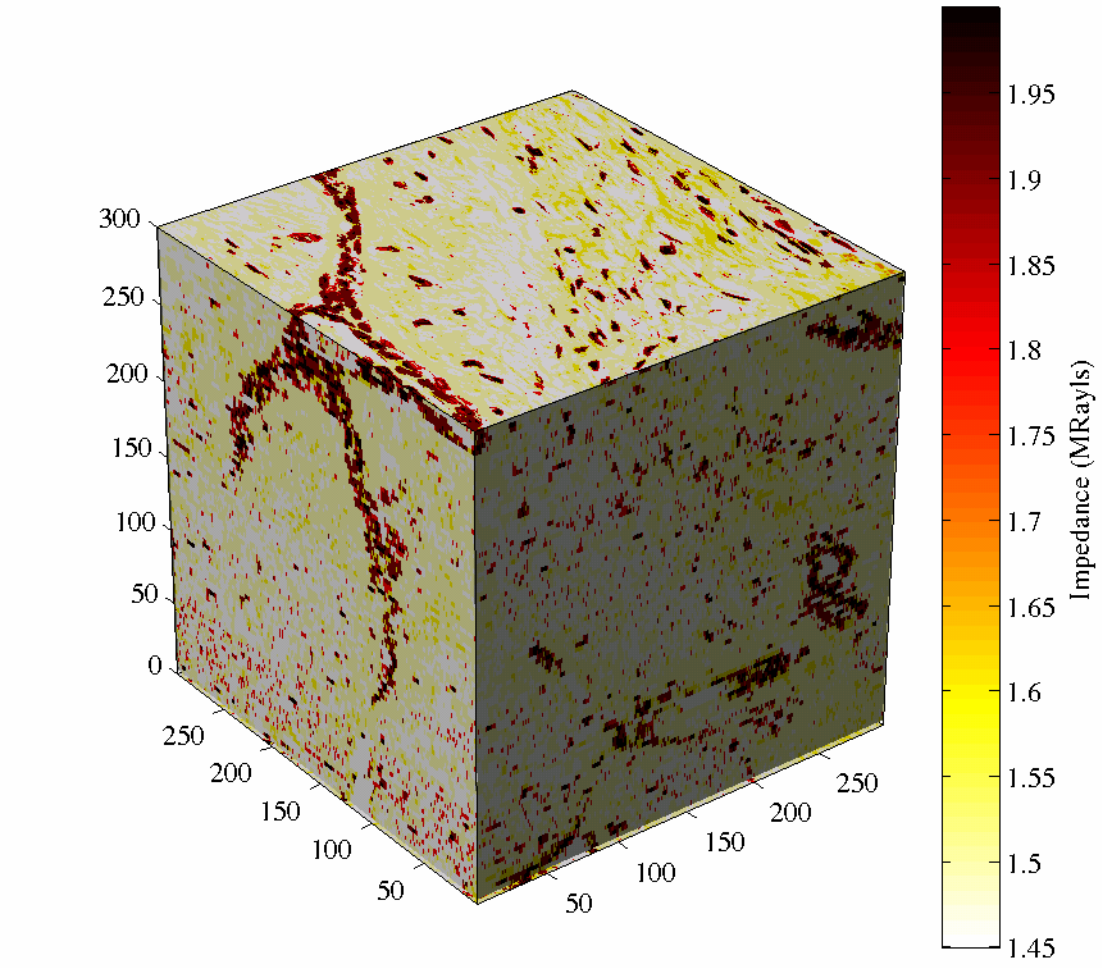

Figure 3.11 3D rendering of WI #53 3DZM.

Results from a second fibroadenoma dataset, called WI #54, are shown in Figure 3.12 and Figure 3.13. Again, the reconstructed faces of the volume appear to show similar structure when compared to the images from the original data set.

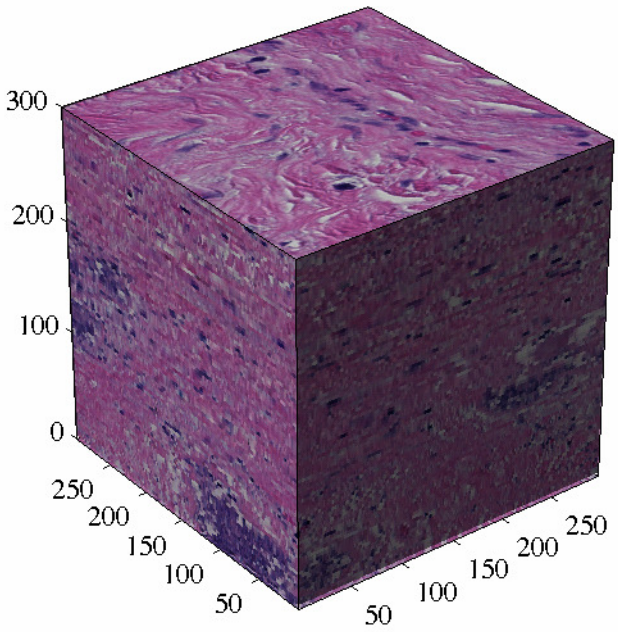

Figure 3.12 3D rendering of WI #54 3DHM.

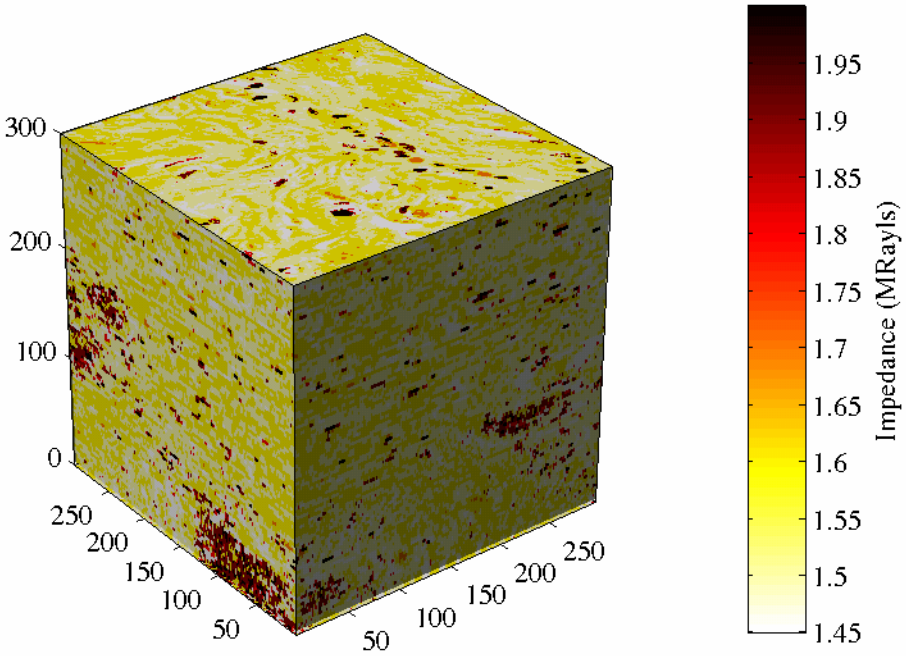

Figure 3.13 3D rendering of WI #54 3DZM.

CHAPTER 4

IMPEDANCE MAP ANALYSIS

As a result of the relationship between backscattered intensity and the squared magnitude of the spatial Fourier transform of a medium's relative impedance function, as dictated by Equations (2.10) and (2.11), 3DZMs present a useful tool for the study of ultrasonic scattering in tissue. This relationship can be exploited in two ways. First, by assuming some form factor model, estimates may be made of parameters like scatterer size and acoustic concentration from a 3DZM. Second, by using the 3DZM to investigate the layout of the tissue microstructure from an acoustic perspective, new scattering models may be developed which better represent the underlying tissue structure.

This chapter presents the techniques and results of 3DZM analysis. First, the principles of estimating the power spectra of 3DZMs are discussed, followed by a discussion of scatterer size estimation from a 3DZM. Finally, the analysis results from a collection of 3DZMs created from human fibroadenomas are presented.

4.1 Spectral Estimation

Spectral estimation refers to the signal processing steps taken to compute the power spectrum of a 3DZM. In this step, the underlying tissue is treated as a random medium, for which it is desired to estimate the statistical power spectrum using the limited spatial samples of the volume.

The 3D spatial Fourier transform of a volume produces a 3D function of the spatial frequency vector $\mathbf{k} = k_x\hat{x} + k_y\hat{y} + k_z\hat{z}$. In the special case of a spherically

symmetric scatterer, the Fourier coefficients along each radial path away from $\mathbf{k} = \vec{0}$ are equal, regardless of which path is chosen; thus, the value of the 3D spatial Fourier transform along any such path is equal to the acoustic form factor of the medium, with the wave number $k = \sqrt{k_x^2 + k_y^2 + k_z^2}$. For an *M*-by-*N*-by-*P*-element 3D volume *f*(*x*,*y*,*z*), the 3D, spatial, discrete Fourier transform is given by

$$F(k_x, k_y, k_z) = \frac{1}{MNP} \sum_{x=0}^{M-1} \sum_{y=0}^{N-1} \sum_{z=0}^{P-1} f(x, y, z) e^{-j2\pi(k_x x + k_y y + k_z z)} . \tag{4.1}$$

The selection of the radial paths for which two of the spatial frequency variables are equal to zero greatly simplifies the computation of this transform. For example, consider the case in which k_y and k_z are equal to zero. Then, Equation (4.1) reduces to

$$F(k_x, 0, 0) = \frac{1}{MNP} \sum_{x=0}^{M-1} \left[\sum_{y=0}^{N-1} \sum_{z=0}^{P-1} f(x, y, z) \right] e^{-j2\pi(k_x x)} \tag{4.2}$$

which is seen to be simply the 1D, spatial, discrete Fourier transform of the double sum term within the brackets.

For an ensemble of randomly positioned, identical spherical scatterers, the coherent scattering term in Equation (2.17) adds random variation to the underlying scattering function. This term is spatially dependent, so different radial paths of the 3D spatial Fourier transform will have different coherent scattering terms. Thus, averaging multiple radial slices of the 3D spatial Fourier transform together serves to reduce the effects of the coherent scattering term. This was done using the three orthogonal radial paths along which $k = k_x$, $k = k_y$, and $k = k_z$ by using an appropriately modified form of Equation (4.2).

A 3DZM presents a finite-duration representation of the underlying medium. If a function $m(x,y,z)$ is defined as an infinite medium containing randomly positioned scatterers, then an M-by-N-by-P-element 3D volume $f(x,y,z)$ can be expressed as the multiplication of this infinite medium with a 3D window function $w(x,y,z)$; that is,

$$f(x, y, z) = m(x, y, z)w(x, y, z). \tag{4.3}$$

In the Fourier domain, this implies that the effect of this windowing operation is the convolution of the original signal spectrum with the spectrum of the window function, so

$$F(k_x, k_y, k_z) = M(k_x, k_y, k_z) * W(k_x, k_y, k_z). \tag{4.4}$$

For this work, a 3D rectangular window was used. However, the proper application of some other windowing function, such as a 3D Hamming window, could be applied to decrease sidelobe contributions while maintaining good spectral resolution [9].

The Fourier transform of Equation (4.2) was implemented using the fast Fourier transform (FFT) algorithm. Zero padding was used to increase the frequency sampling, but this required that the signal be zero-mean. Thus, for the computation of Equation (4.2) using a zero-padded FFT, the mean of the windowed signal was subtracted from each element. In the Fourier domain, this only affects the zero-frequency component, which is not relevant to the analysis of 3DZMs. If this value were needed, it could be computed as the mean value of the 3D windowed signal, as indicated by evaluating Equation (4.1) with $\mathbf{k} = \vec{0}$.

4.2 Scatterer Size Estimation

Scatterer size estimation is the task of fitting the deduced form factor of a 3DZM to a theoretical FF to produce an estimate of the effective scatterer diameter. FFs of

spherically symmetric scatterers, like the fluid-filled sphere FF described by Equation (2.12), have a frequency dependence which scales depending only on the scatterer size. Thus, a best-fit curve is used to determine the scatterer size estimate using a particular theoretical FF.

An estimation scheme for 3DZMs has been developed previously by Mamou [1] and is summarized here. This scheme produces an estimate a^* of scatterer radius by minimizing the mean squared error (MSE) between the log of the deduced FF and the log of the theoretical FF scaled by a gain term over some frequency range $k_{\min}$ to $k_{\max}$. For discrete functions, this MSE is expressed as

$$MSE(a, k_{\min}, k_{\max}) = \frac{1}{k_{\max} - k_{\min}} \sum_{k=k_{\min}}^{k_{\max}} \left[\log(S(2k)) - \log(G_a F_a(2k))\right]^2 \tag{4.5}$$

where $S(2k)$ is the deduced FF of a 3DZM, $F_a(2k)$ is a theoretical FF for radius a, and G_a is an estimated gain term computed as

$$\log(G_a) = \sqrt{\frac{1}{k_{\max} - k_{\min}} \sum_{k=k_{\min}}^{k_{\max}} \left|\log(S(2k)) - \log(F_a(2k))\right|^2}\,. \tag{4.6}$$

This gain term is an estimate of the proportionality factor between the theoretical FF and the deduced FF. It can be related to a parameter called *acoustic concentration* [1], which relates to the number density and scattering strength of the scatterers. While acoustic concentration is a useful and important parameter, this work focused on scatterer size.

This estimation scheme requires the selection of values for the maximum and minimum spatial frequencies $k_{\min}$ and $k_{\max}$. For the optimal value of a, it is desired that the range of the product ka be between 0.5 and 2.0 [11]. However, this optimal value of a is unknown. Thus, to generate estimates that are not biased by the chosen frequency range, an error function was defined as

$$Err(a) = \max\left\{E(a, k_{\text{start}}, \Delta k) \text{ for each } k_{\text{start}} \text{ and } \Delta k\right\} \tag{4.7}$$

where

$$E(a, k_{\text{start}}, \Delta k) = MSE(a, k_{\text{start}}, k_{\text{start}} + \Delta k). \tag{4.8}$$

Then, to enforce the desired *ka* range, $E(a,k_{\text{start}},\Delta k)$ is set to zero if $k_{\text{start}} a < 0.5$ or $(k_{\text{start}} + \Delta k)a > 2.0$. Using this scheme, the estimate a^* is then defined as

$$a^* = \arg\min E(a, k_{\text{start}}, \Delta k). \tag{4.9}$$

Scatterer size estimation was applied to subvolumes of each 3DZM called regions of interest (ROIs). For a given 3DZM, the entire volume was first treated as the ROI. Each dimension of the volume was then divided in half, and the eight resulting subvolumes were analyzed as ROIs. This process of dividing each volume into eight subvolumes could continue until each ROI consisted of only a single voxel; in this work, 3DZMs were never divided into more than 64 subvolumes.

4.3 Simulations

Simulated 3DZMs were used to test the analysis techniques described in this chapter. These simulations were designed to investigate several aspects of the 3DZM analysis techniques, especially the effect of ROI size and the effect of non-spherical scatterers on the size estimates. Ultimately, the goal of these simulations was to obtain a better understanding of the relationship between the analysis results and the physical properties of the 3DZM.

4.3.1 Simulation methods

The simulated 3DZMs used in this study consisted of fluid-filled scatterers that were randomly positioned in a background medium. Fluid-filled spheres (or spheroids) were used because they are very simple to generate and are compactly supported (as opposed to, for example, Gaussian scatterers which have an infinite support). All analyses were performed using the fluid-filled sphere form factor model.

Simulated 3DZMs were generated using a simple process. First, the number of scatterers in the volume was defined, along with the size and impedance of each scatterer. Next, the spatial locations of the scatterers were randomly generated, and finally a computational volume was created with scatterers in the specified positions. The spatial locations of the scatterers were generated by drawing the coordinates of the scatterer center from a uniform probability distribution. The coordinates of the n^{th} scatterer were then tested against all preceding scatterers to ensure that no scatterers were overlapping. This was done by computing the distance between the most recently generated scatterer and each previous scatterer. Then, the new coordinates were rejected if this distance was less than the sum of the respective scatterer radii (or an equivalent dimension for non-spherical scatterers). That is, the condition

$$\left\| x_n - x_k \right\| \geq r_n + r_k \tag{4.10}$$

was enforced for $k = 1, \ldots, n\text{-}1$, where x_k and r_k denote the spatial location and radius, respectively, of the k^{th} scatterer. If a scatterer location was generated which did not satisfy this condition, it was rejected and a new location was generated and tested.

Several studies were performed using simulated 3DZMs. Each study was performed by simulating and analyzing 50 3DZMs of dimensions 300x300x300 μm. In

the first study, each 3DZM contained 20 spheres of radius 25 μm. This study was performed to validate the estimation routine for a simple case and to test the effect of ROI size on the results. In the second study, two sphere sizes were used: 10 spheres of radius 25 μm and 40 spheres of radius 8 μm. Again, this was performed to investigate the effect of ROI size on the scatterer size estimate results. The third study used prolate spheroidal scatterers (shaped like a grain of rice). In this case, the scatterers had a 25 μm radius on the major axis and a 15 μm radius on each of the minor axes, and 40 scatterers were placed in each volume. The scatterers were placed in the volume at random orientations. The fourth study used oblate spheroidal scatterers, which are slightly flattened versions of the prolate spheroids, with axial radii of 35 μm, 15 μm, and 10 μm. Finally, the fifth study used very long, narrow prolate spheroids with a major axis length which was greater than the dimensions of the volume and a minor axis radius of 10 μm. This appeared roughly as cylindrical scatterers which passed through the volume. For this study, the scattering structures were allowed to intersect within the volume.

4.3.2 Simulation results

The first study consisted of simulated 3DZMs containing 20 randomly placed, spherical scatterers of radius 25 μm. Figure 4.1 shows a histogram of the results obtained using the entire volume as the ROI. Figure 4.2 and Figure 4.3 show the histograms of the results obtained by dividing each volume into 8 and 64 subvolumes, respectively.

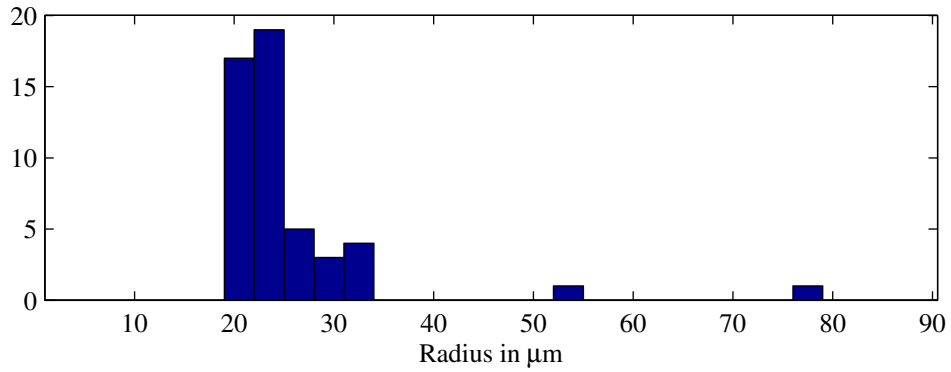

Figure 4.1 Histogram of scatterer radius estimates obtained using the entire volume as the ROI for a collection of identical, spherical scatterers of radius 25 µm.

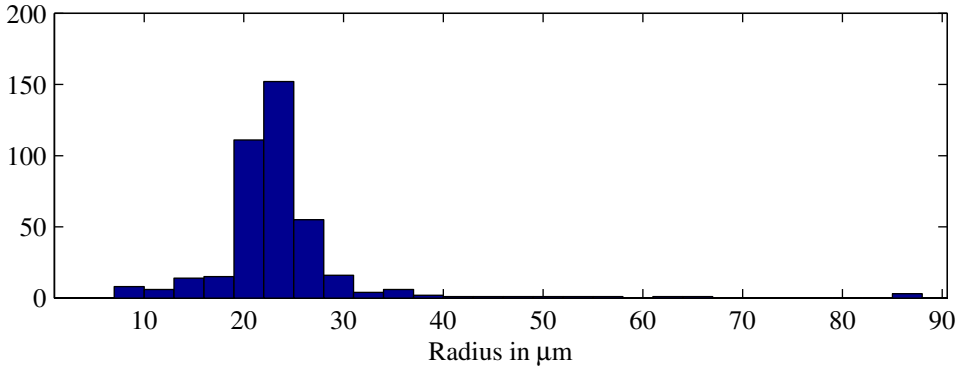

Figure 4.2 Histogram of scatterer radius estimates obtained by dividing each 3DZM into eight subvolumes for a collection of identical, spherical scatterers of radius 25 µm.

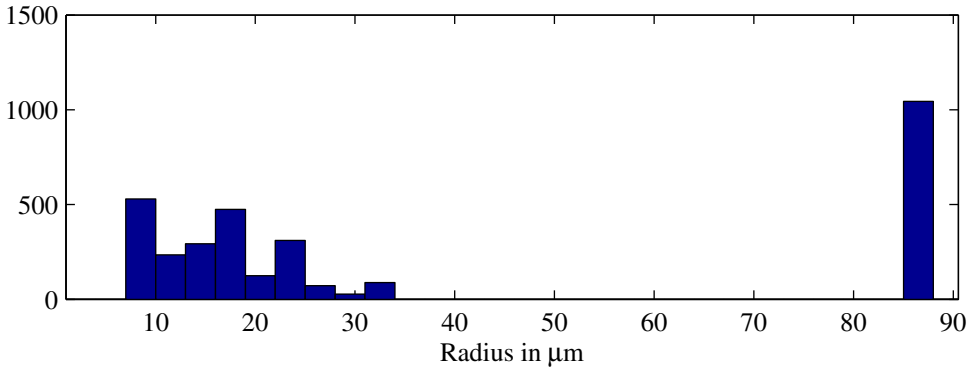

Figure 4.3 Histogram of scatterer radius estimates obtained by dividing each 3DZM into 64 subvolumes for a collection of identical, spherical scatterers of radius 25 µm.

As shown in Figure 4.1, the estimates obtained when using the entire volume as the ROI are tightly clustered around the true value of 25 µm. Any deviation from this value can be attributed to the effect of spheres which intersect the boundary of the

volume. Figure 4.2 shows a similar distribution, since the ROI size of 150x150x150 μm is still sufficient to completely contain several scatterers of radius 25 μm. However, Figure 4.3 shows that the smaller 75x75x75 μm ROIs produced much less reliable results. Although this ROI is large enough to fully contain a scattering structure, it is likely that most ROIs contained only portions of scattering structures, resulting in the wide range of estimates. In particular, the large spike of estimates at the upper end of the scatterer size range is likely the result of erroneous estimates obtained when no scatterers were present within the ROI. Thus, it is seen that ROI size can affect the estimate results, especially when the ROI size is near to the size of the scatterers.

The second study consisted of simulated ROIs containing scatterers of both 25 μm and 8 μm. The number density of the smaller spheres was four times that of the larger spheres. Figure 4.4 shows the results obtained using the entire volume as the ROI, Figure 4.5 shows the results obtained using 8 subvolumes, and Figure 4.6 shows the results obtained using 64 subvolumes.

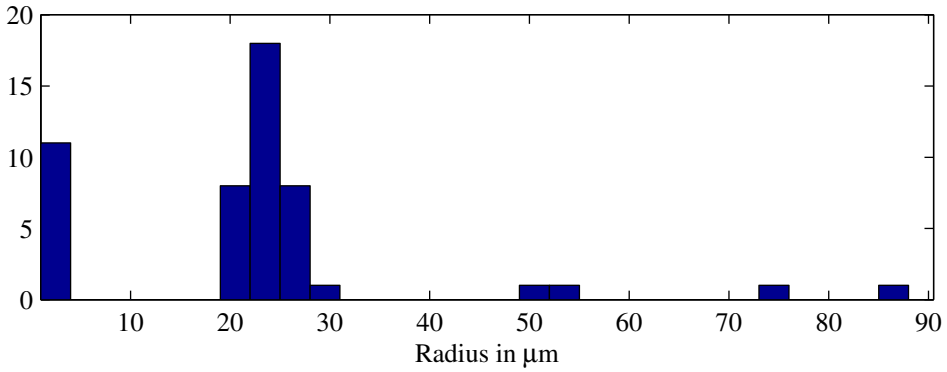

Figure 4.4 Histogram of scatterer radius estimates obtained using the entire volume as the ROI for a collection of spherical scatterers with radii 25 μm and 8 μm.

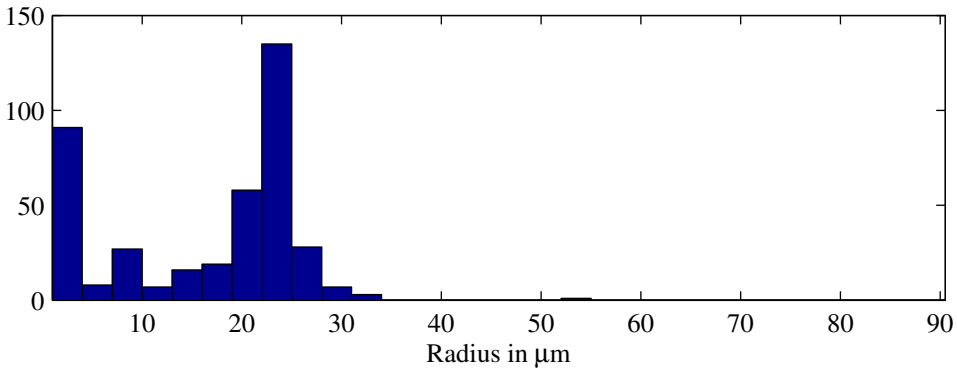

Figure 4.5 Histogram of scatterer radius estimates obtained by dividing each 3DZM into eight subvolumes for a collection of spherical scatterers with radii 25 µm and 8 µm.

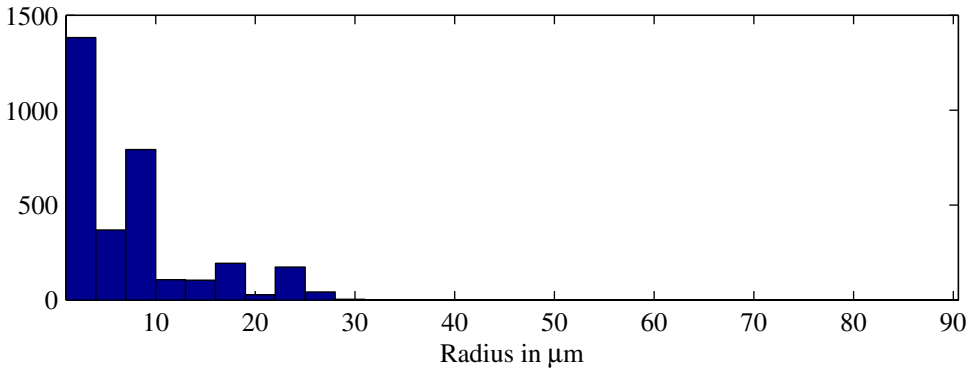

Figure 4.6 Histogram of scatterer radius estimates obtained by dividing each 3DZM into 64 subvolumes for a collection of spherical scatterers with radii 25 µm and 8 µm.

Again, these figures demonstrate the dependence of the estimates on the ROI size. It is seen that the estimates from the smallest ROIs tend toward the smaller scattering structures, while the estimates from the larger ROIs tend toward the larger scattering structures. Additionally, several outlying results are seen, including many estimate results in the smallest bin of each histogram. This demonstrates how deviation from the simple case presented in the first study can produce some unwanted results. The situation is further complicated by the intersection of some scattering structures with the boundary of the volume.

The third study used non-spherical scatterers. Prolate spheroids were used, with a major axis radius of 25 µm and a minor axis radius of 15 µm. Each scatterer was placed

with a random orientation. Figure 4.7 shows a 3D rendering of a sample scattering volume.

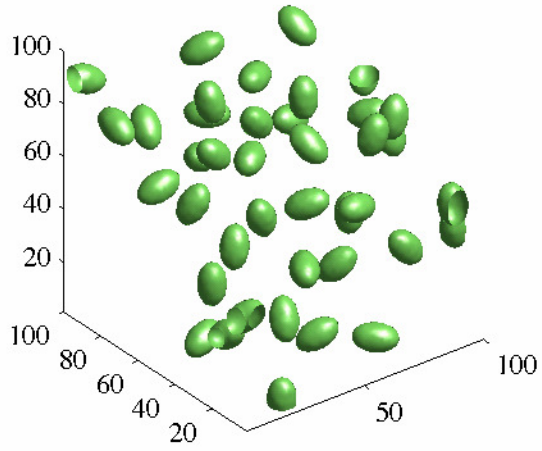

Figure 4.7 Scattering volume example for the prolate spheroid scatterers used in the third study.

Figure 4.8 shows the estimation results obtained using the entire volume as the ROI, Figure 4.9 shows the results obtained using 8 subvolumes, and Figure 4.10 shows the results obtained using 64 subvolumes.

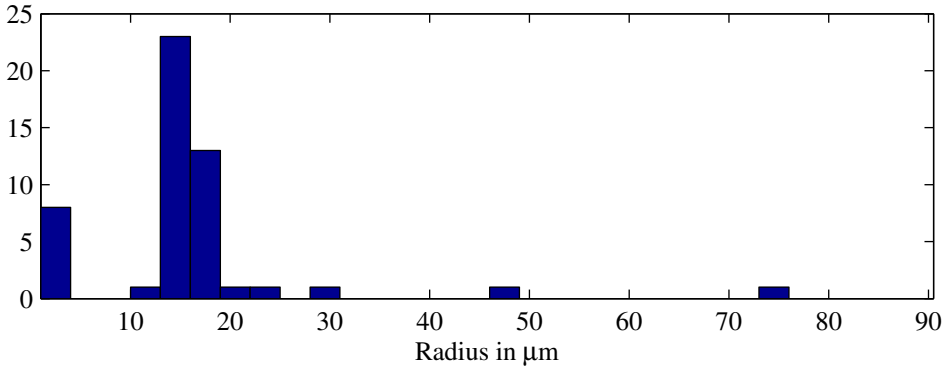

Figure 4.8 Histogram of scatterer radius estimates obtained using the entire volume as the ROI for a collection of prolate spheroidal scatterers with a major axis radius of 25 µm and a minor axis radius of 15 µm.

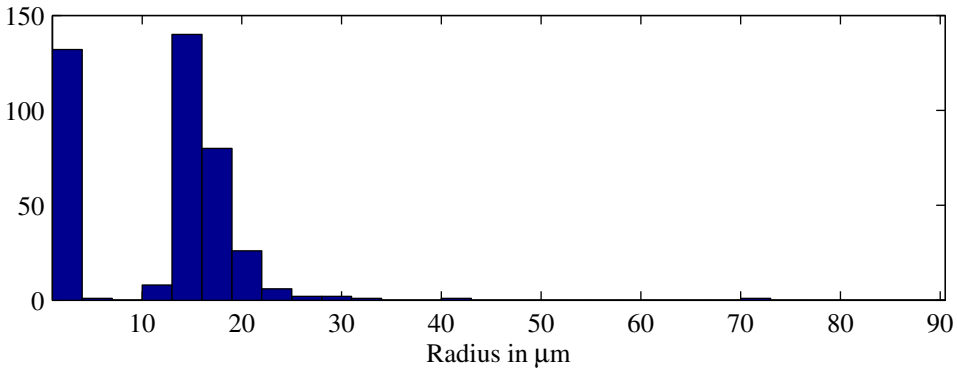

Figure 4.9 Histogram of scatterer radius estimates obtained by dividing each 3DZM into eight subvolumes for a collection of prolate spheroidal scatterers with a major axis radius of 25 μm and a minor axis radius of 15 μm.

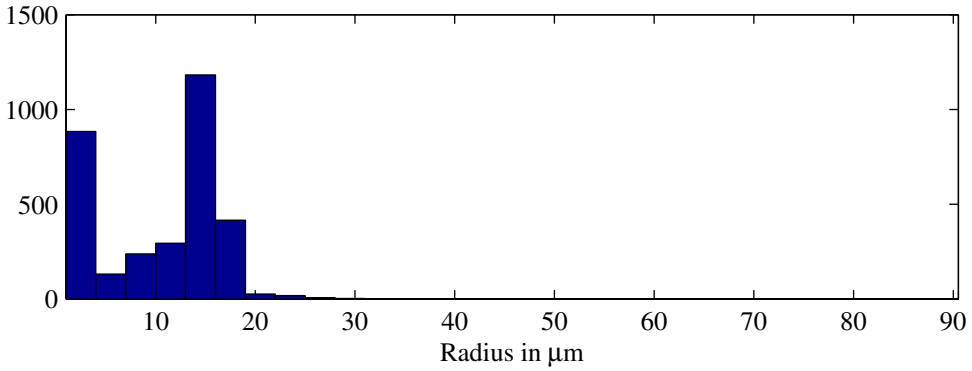

Figure 4.10 Histogram of scatterer radius estimates obtained by dividing each 3DZM into 64 subvolumes for a collection of prolate spheroidal scatterers with a major axis radius of 25 μm and a minor axis radius of 15 μm.

In this situation, it is seen that the estimation results tend to fall between the major and minor axis dimensions when the size estimates are made using a spherical scattering model. This is an interesting result, since the assumption of spherically symmetric scatterers is probably untenable in actual tissue. Thus, this provides some insight into the interpretation of estimation results obtained from actual tissue data. Again, however, a large number of ROIs produce a meaningless estimate at the extreme low end of the size spectrum.

The fourth study also used non-spherical scatterers. In this case, the scatterers were oblate spheroids, having three unequal axis lengths. The scatterer size was selected to be slightly more eccentric than the scatterers used in the third study; the axis radii were set to 35 μm, 15 μm, and 10 μm. Again, the scatterers were placed with random orientations within the volume. Figure 4.11 shows a 3D rendering of a sample scattering volume.

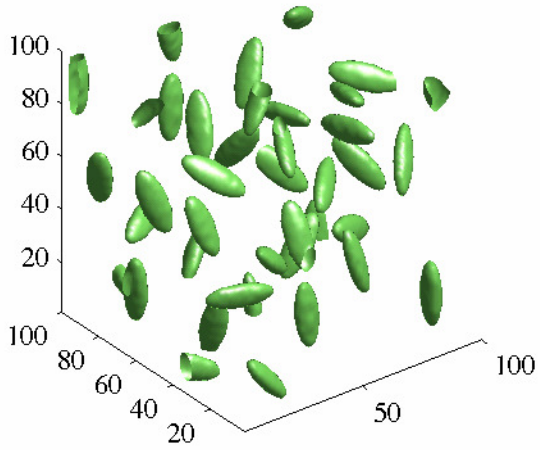

Figure 4.11 Scattering volume example for the oblate spheroid scatterers used in the fourth study.

Figure 4.12 shows the results obtained using the entire volume as the ROI, Figure 4.13 shows the results obtained using 8 subvolumes, and Figure 4.14 shows the results obtained using 64 subvolumes.

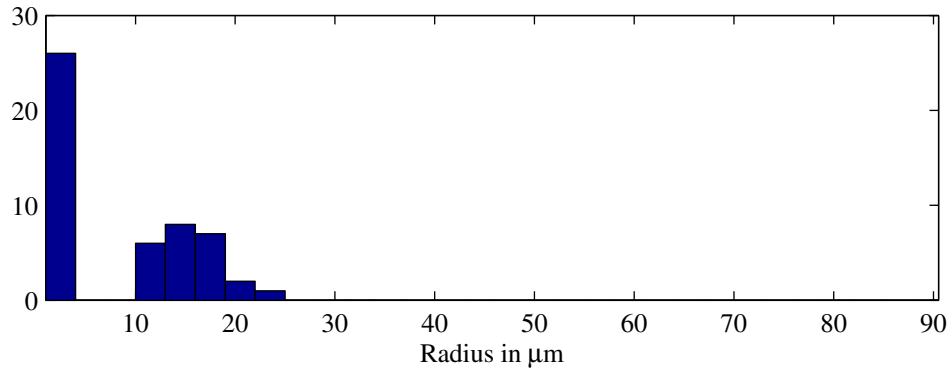

Figure 4.12 Histogram of scatterer radius estimates obtained using the entire volume as the ROI for a collection of oblate spheroidal scatterers with axis radii of 35 µm, 15 µm, and 10 µm.

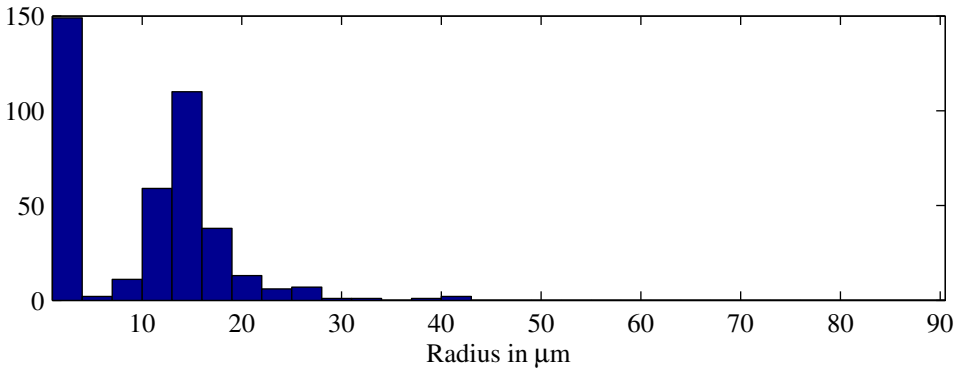

Figure 4.13 Histogram of scatterer radius estimates obtained by dividing each 3DZM into eight subvolumes for a collection of oblate spheroidal scatterers with axis radii of 35 µm, 15 µm, and 10 µm.

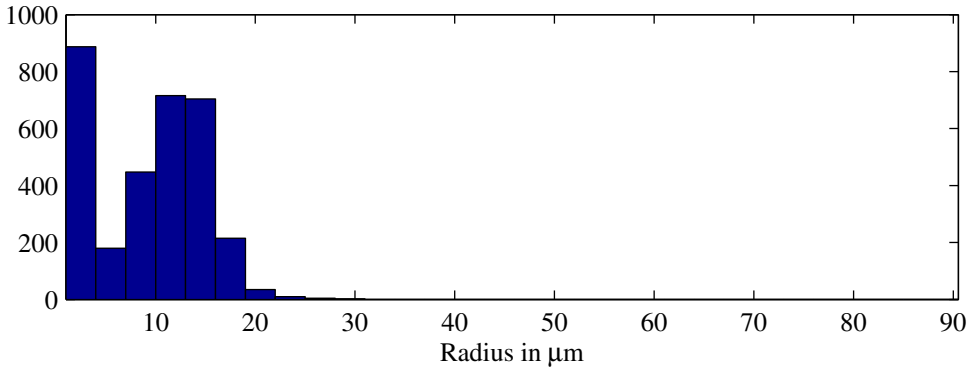

Figure 4.14 Histogram of scatterer radius estimates obtained by dividing each 3DZM into 64 subvolumes for a collection of oblate spheroidal scatterers with axis radii of 35 µm, 15 µm, and 10 µm.

Interestingly, excluding the results at the extreme low end of the size spectrum, the results in this case are seen to fall primarily between the dimensions of the two smaller axes, with few estimates near the dimension of the major axis. This suggests that as the scatterers become more eccentric, the estimates are not strongly biased toward the largest dimension of the scatterer, but rather toward the compact, central portion of the scatterer. This trend was visible for every ROI size, even though the major axis size of the scatterers was nearly equal to the dimensions of the smallest ROIs.

The fifth study used prolate spheroidal scatterers with a major axis radius which was much larger than the volume. The minor axis radius was set to 10 μm. Thus, each volume appeared to contain a web of cylindrical scatterers with random orientation within the volume. The scatterers were allowed to intersect for this study. Figure 4.15 shows an example scattering volume.

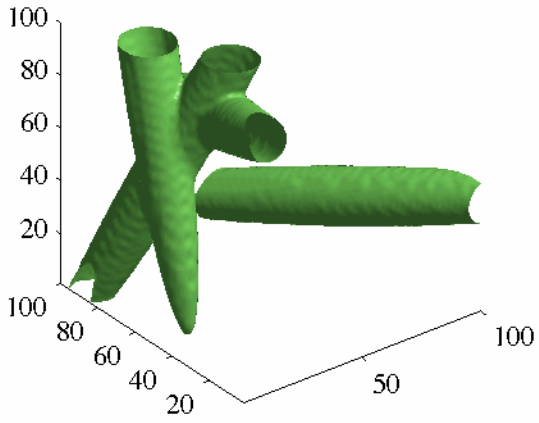

Figure 4.15 Scattering volume example for the web of prolate spheroidal scatterers used in the fifth study.

Figure 4.16 shows the results obtained using the entire volume as the ROI, Figure 4.17 shows the results obtained using 8 subvolumes, and Figure 4.18 shows the results obtained using 64 subvolumes.

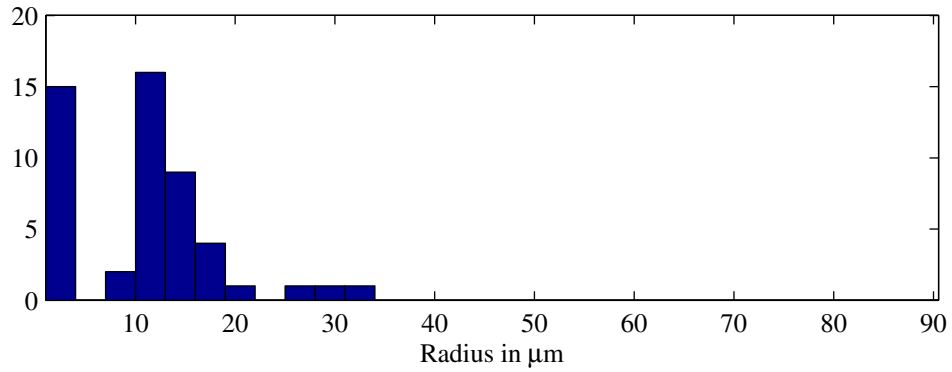

Figure 4.16 Histogram of scatterer radius estimates obtained using the entire volume as the ROI for a web of prolate spheroidal scatterers with a minor axis radius of 10 µm.

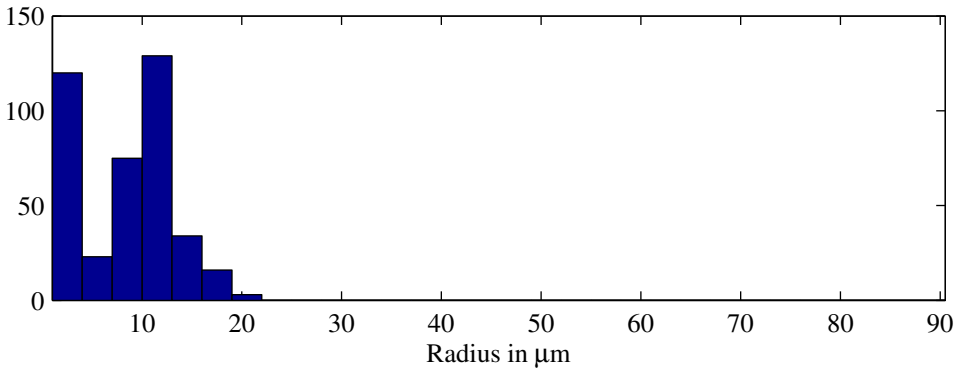

Figure 4.17 Histogram of scatterer radius estimates obtained by dividing each 3DZM into eight subvolumes for a web of prolate spheroidal scatterers with a minor axis radius of 10 µm.

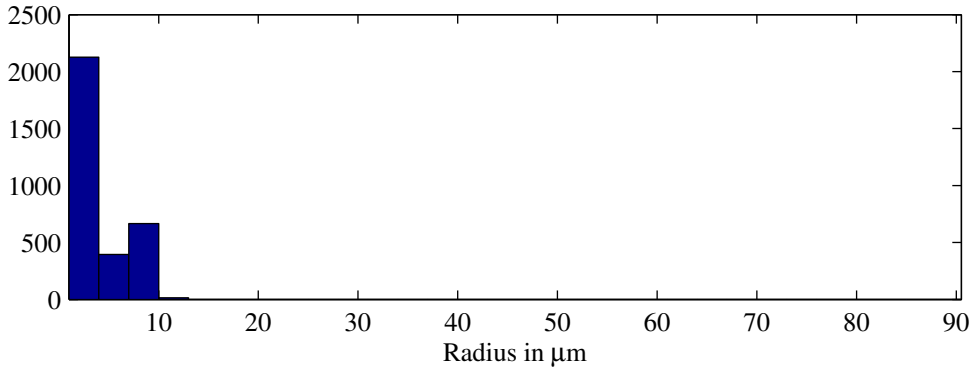

Figure 4.18 Histogram of scatterer radius estimates obtained by dividing each 3DZM into 64 subvolumes for a web of prolate spheroidal scatterers with a minor axis radius of 10 µm.

In this case, the results are seen to fall roughly within the range of the minor axis radius, especially for the larger ROI sizes. Again, this provides some interesting insight into the estimation results obtained from volumes containing randomly positioned, randomly oriented, non-spherical scatterers.

4.4 Fibroadenoma Analysis Results

The collection of human fibroadenoma 3DZMs described in Section 3.6 was analyzed with the techniques set forth in this chapter. Size estimates were obtained using the fluid-filled sphere form factor model. Figure 4.19 shows a histogram of the size estimates obtained by using the entire 3DZM as the ROI; Figure 4.20 shows a histogram of the size estimates obtained by using eight ROIs, formed by dividing each dimension of the 3DZM in half.

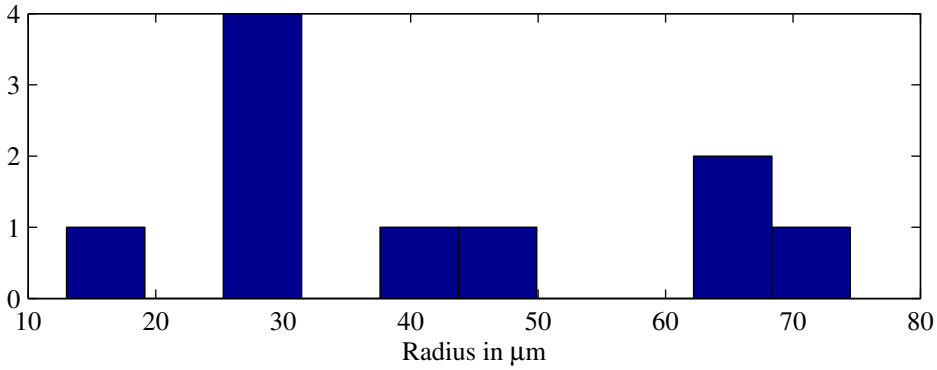

Figure 4.19 Histogram of scatterer size estimates obtained from 10 human fibroadenoma 3DZMs using the entire 300x300x300 μm volume for ROIs.

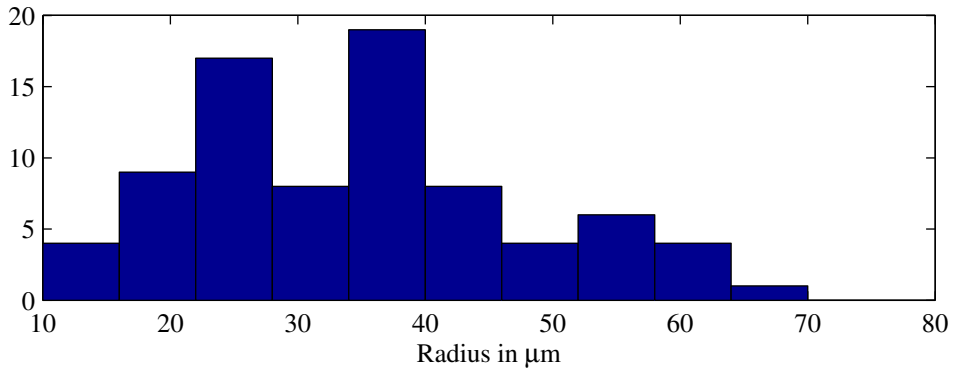

Figure 4.20 Histogram of scatterer size estimates obtained from 10 human fibroadenoma 3DZMs using 150x150x150 µm subvolumes for ROIs.

For estimates made using the entire volume as the ROI, a mean scatterer radius of 42 µm was obtained, with a standard deviation of 20 µm. For estimates made using eight ROIs with dimensions equal to half those of the entire volume, a mean radius of 35 µm and a standard deviation of 15 µm was obtained. Table 4.1 displays the scatterer radius estimation results for each of the 3DZMs analyzed.

Table 4.1 3DZM scatterer size estimation results.

3DZM name	**300x300x300 µm ROI estimation results (µm)**	**150x150x150 µm ROIs estimation results (µm)**
WI #50 3DZM 1	42.5	39.7 ± 14.0
WI #51 3DZM 1	62.5	36.5 ± 14.3
WI #51 3DZM 2	13.0	29.4 ± 9.4
WI #52 3DZM 1	28.5	34.1 ± 12.9
WI #53 3DZM 1	28.5	27.6 ± 11.0
WI #54 3DZM 1	74.5	39.5 ± 18.5
WI #55 3DZM 1	68.0	32.6 ± 11.3
WI #56 3DZM 1	31.0	33.6 ± 9.9
WI #57 3DZM 1	45.5	38.9 ± 10.3
WI #58 3DZM 1	26.0	36.6 ± 16.9

The scatterer radius estimates presented in Table 4.1 were obtained by assuming a fluid-filled sphere as a scattering model. Thus, the physical meaning of the results depends on how well the actual scattering sites can be approximated as fluid-filled

spheres; some insight into this interpretation was provided by the simulations in the previous section. The results from several fibroadenoma samples are presented here, and the estimates from each of these cases are then compared to the histological features of the samples. First, the results from the datasets previously presented in Chapter 3 (WI #53 and WI #54) are discussed, followed by the results from WI #55.

Figure 4.21 shows a histological image section from the WI #53 dataset. Figure 4.22 shows a visualization of the surfaces within the 3DZM which have impedance values between 1.8 and 2.0 Mrayls. From these figures, it can be seen that the most prominent features within the volume appear to be the curvilinear duct formations (the dark, web-like structures in Figure 4.21). As indicated by Table 4.1, the scatterer radius estimates derived from this 3DZM are about 28 μm for both ROI sizes (that is, a diameter of about 56 μm). From these figures, it is difficult to identify any structures within the volume which are on the scale of this size estimate, especially structures which could be approximated in some way as fluid-filled spheres. The simulation results suggest that this value may represent an estimate of the minor dimension of these duct formations, although this is difficult to determine from the histological data.

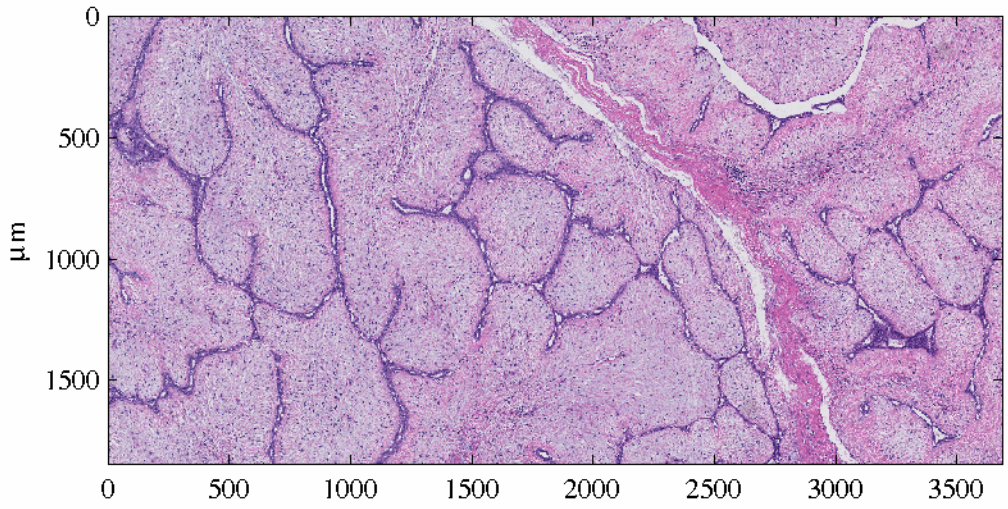

Figure 4.21 Histological image of WI #53 fibroadenoma.

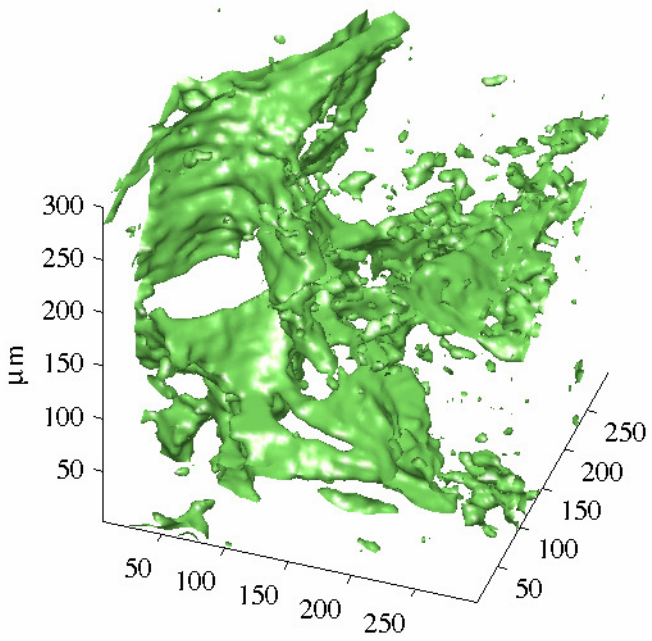

Figure 4.22 Surfaces in WI #53 3DZM with impedance values in the range of 1.8 to 2.0 Mrayls.

Other datasets do appear to have structure which agrees with their respective scatterer size estimates. Figure 4.23 shows a histological image from the WI #54 dataset, Figure 4.24 shows a magnified view of a histological image, and Figure 4.25 shows a

view of the 3DZM surfaces with impedance values between 1.8 and 2.0 Mrayls. In this case, the estimated scatterer diameter was 149 μm when the entire volume was used as the ROI, and 79 μm when the volume was divided into eight smaller ROIs. The acini (dark cell clusters in Figure 4.23) appear to have dimensions which are, in some cases, consistent with these size estimates. In Figure 4.23, it can be seen that some of these acini appear to have dimensions which are even larger than 149 μm. Presumably, this is a result of the ROI size and the fact that only a single 3DZM was used to make these estimates. Similarly, the reduction in estimated scatterer size which accompanies the use of smaller ROIs is likely an issue of scale as well, since it is unlikely that a scatterer with a size on the order of 150 μm will be present within a 150x150x150 μm ROI. This effect of ROI size was also observed in simulations.

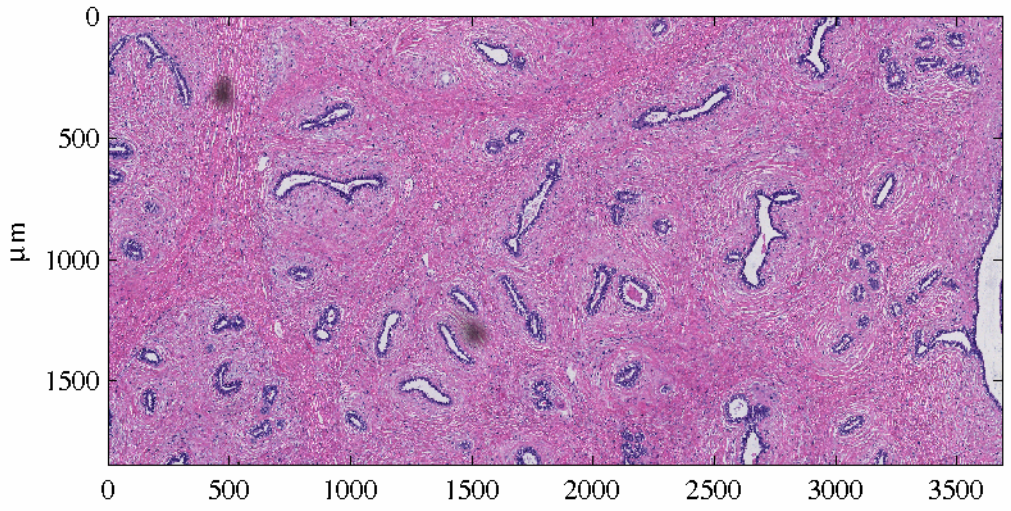

Figure 4.23 Histological image of WI #54 fibroadenoma.

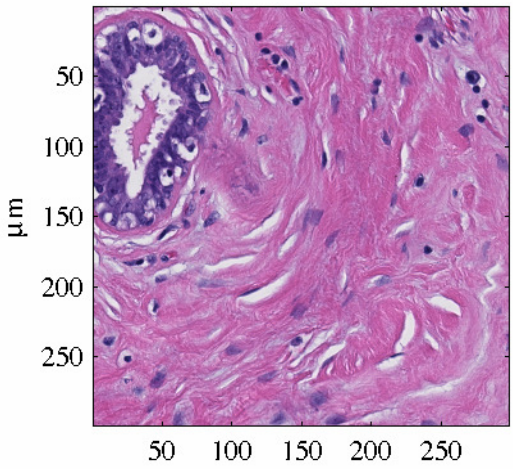

Figure 4.24 Magnified view of WI #54 fibroadenoma showing structure on the scale of the computed scatterer size estimates. An acinus is visible in the upper left corner.

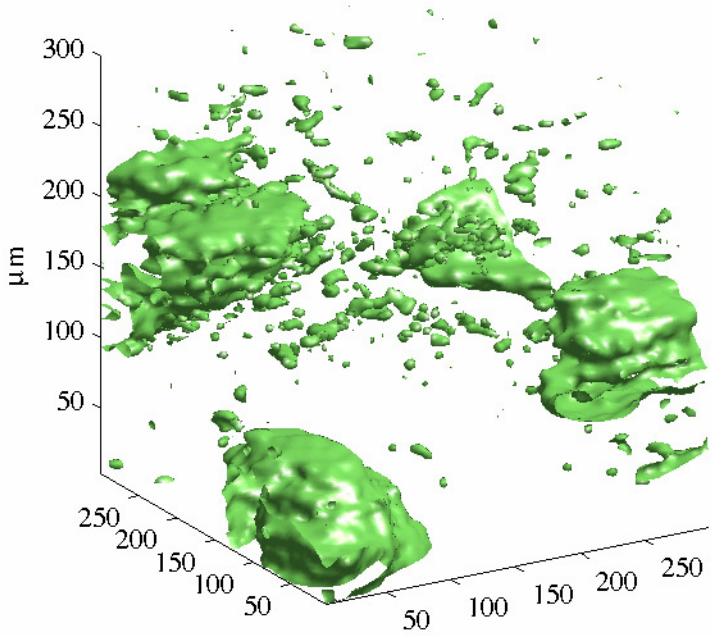

Figure 4.25 Surfaces in WI #54 3DZM with impedance values in the range of 1.8 to 2.0 Mrayls.

The WI #55 tumor images show similar structure to that of WI #54, although the acini appear to be slightly smaller and more densely packed. Figure 4.26 shows a histological image, while Figure 4.27 shows the surfaces in the 3DZM with impedance values between 1.8 and 2.0 Mrayls. The scatterer diameter estimates are similar to those

made for WI #54: 136 µm using the entire volume, and 75 µm using eight subvolumes. Again, these estimates seem to be reasonable when the ROI size is considered. Thus, this suggests that the acini may be the dominant scattering structures within this tissue volume.

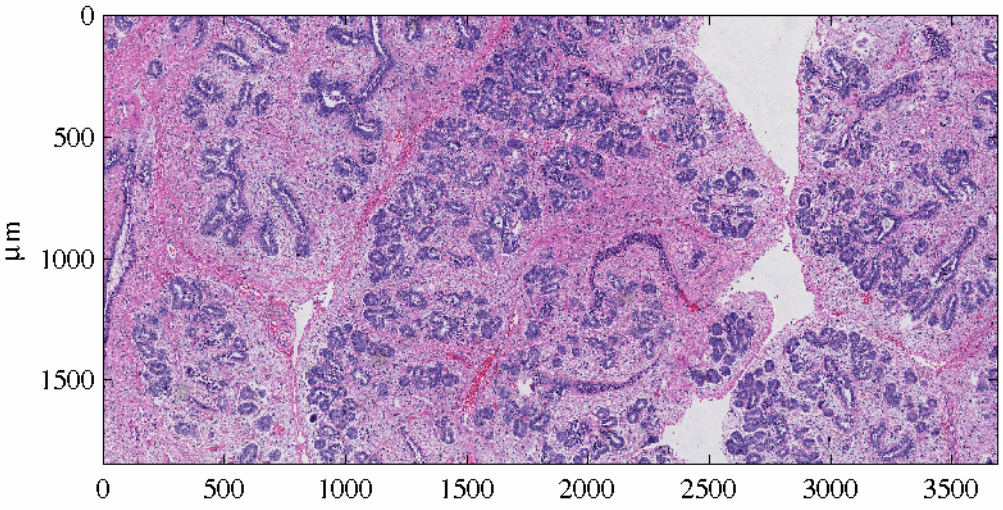

Figure 4.26 Histological image of WI #55 fibroadenoma.

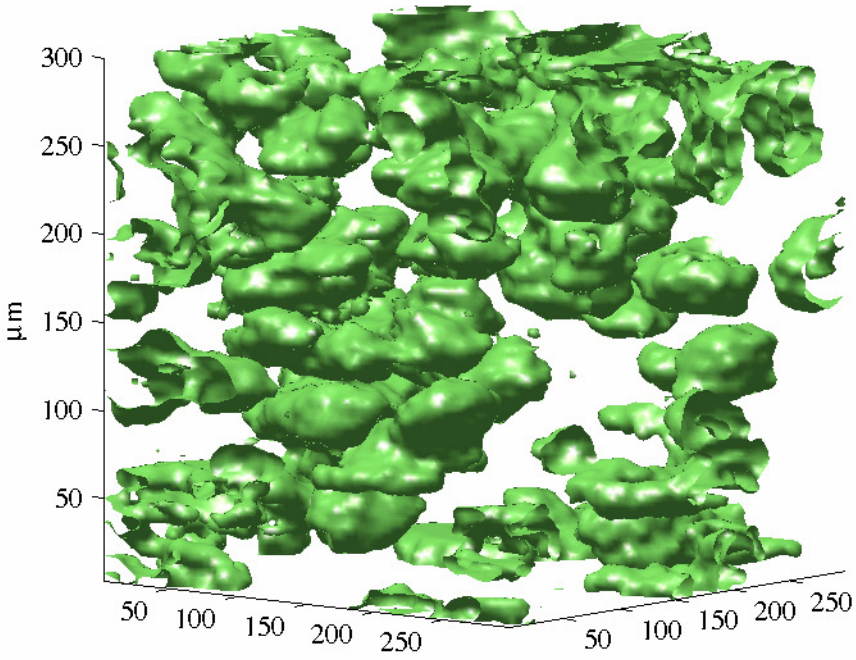

Figure 4.27 Surfaces in WI #54 3DZM with impedance values in the range of 1.8 to 2.0 Mrayls.

CHAPTER 5
DISCUSSION

5.1 Three-Dimensional Impedance Map Construction

The results presented in Chapter 3 demonstrate the effectiveness of the current scheme in which histological images, generated by the NanoZoomer, are processed into a 3DZM. This process is almost entirely automated, allowing 3DZMs to be created quickly and easily when new data sets are available. Also, because the raw tissue images are much larger than the 3DZMs that were presented here, many 3DZMs can be created from a single data set.

As in the previous work [1], computational efficiency was not a primary concern in the development of these 3DZM creation routines. A reduction in the computation needed for 3DZM creation would be useful, although not strictly necessary. Faster computation would enable larger 3DZMs to be made more easily, which would improve tissue analysis using 3DZMs.

Validation of the 3DZM construction process remains an important challenge. To some degree, the proper registration of the tissue sections can be confirmed visually by viewing the histological maps in a variety of ways. For example, the stacked images can be viewed as a 3D volume; histological images can be formed by slicing the 3D volume vertically; or, each slice can be viewed sequentially as a movie. While none of these techniques can be used to quantitatively validate the agreement between the histological map and the original tissue volume, they do provide a means to easily identify when registration has clearly failed, and they also provide a qualitative means to evaluate the

registration results. A more quantitative method which could be used to validate the 3DZM construction process would be the comparison of spectra obtained from 3DZMs with spectra obtained using ultrasonic interrogation of the same medium. This comparison would be most effective if it were done using multiple 3DZMs created from the medium, rather than using only a single sample, so that an average spectrum from the medium could be obtained.

The assignment of impedance values is a critical step in the process of 3DZM creation, and as such it merits further investigation. As suggested in [1], an iterative method could be used to adjust the impedance values until agreement with some reference was obtained. For example, consider a 3DHM which has been assembled from tissue data for which ultrasonic backscatter measurements also exist. The impedance values could be set to initial values and the spectrum of the resulting 3DZM could be compared to the spectrum of the ultrasonic data using some similarity metric. Based on this comparison, the impedance values could be adjusted, and the spectrum of the resulting 3DZM could again be compared to the ultrasonic spectrum. This process could iterate until convergence of the spectra is obtained. The HSI colorspace presents a simple framework for this adaptation, since the impedance values, threshold levels, or both could be used as adjustable parameters.

5.2 Three-Dimensional Impedance Map Analysis

The analysis of human fibroadenoma 3DZMs, as presented in Chapter 4, demonstrates the application of 3DZMs as a tool for the study of ultrasonic scattering in tissue. In some cases, the scatterer size estimates derived using the fluid-filled sphere

form factor provided a means to identify histological tissue structures which could serve as the dominant scattering source in this tissue. Still, certain adjustments to the analysis process could be made to improve upon these results.

Larger 3DZMs would be beneficial because more scattering structures and larger scattering structures could be contained within the 3DZM. An effect was seen in some of the analysis results (WI #54 and WI #55, see Table 4.1) where a reduction in the ROI dimensions from 300 μm cubes to 150 μm produced a corresponding drop in estimated scatterer dimensions. However, in the cases where this effect was present, the estimated scatterer diameter from the larger ROI was approximately equal to the size of the smaller ROIs. Thus, the use of larger 3DZMs would facilitate the recognition of larger scattering structures, if present.

The creation of many 3DZMs from a single dataset would improve the process of tissue analysis. Each 3DZM provides only a relatively small sample of the tissue volume. However, the size of the NanoZoomer images would allow a large number of 3DZMs (10 or more) to be made from the same dataset. This would provide many estimates of the scatterer properties, resulting in a better understanding of the statistical tissue properties.

5.3 Conclusion

3DZMs are a unique tool for the study of ultrasonic scattering in tissue. The ability to easily create 3DZMs from NanoZoomer data was demonstrated, and some analysis techniques and applications of the resulting 3DZMs were explored. Many interesting challenges still remain with regards to 3DZM creation and analysis, but the fibroadenoma results presented here are promising.

This work focused on the specifics of 3DZM creation and analysis. These techniques were demonstrated on a set of 10 3DZMs created from human fibroadenomas; the results were then used to identify possible ultrasonic scattering sources. As this work continues, additional datasets for which both ultrasonic measurements and 3DZMs are available will provide a means to validate the 3DZM creation process. Additionally, such datasets would allow the use of adaptive methods for impedance value assignment.

Quantitative ultrasound holds great diagnostic potential, and 3DZMs provide a powerful means to relate QUS results to actual tissue microstructure. That is, 3DZMs allow a connection to be made between QUS parameters and tissue pathology. This connection could be an essential step to propel QUS forward as an effective and noninvasive diagnostic imaging modality.

REFERENCES

[1] J. Mamou, "Ultrasonic characterization of three animal mammary tumors from three-dimensional acoustic tissue models," Ph.D. dissertation, University of Illinois at Urbana-Champaign, Urbana, IL, 2005.

[2] R. S. C. Cobbold, *Foundations of Biomedical Ultrasound*. New York, NY: Oxford University Press, 1997.

[3] M. L. Oelze, W. D. O'Brien, Jr., and J. F. Zachary, "Quantitative ultrasound assessment of breast cancer using a multiparameter approach," in *Proceedings of the 2007 IEEE Ultrasonics Symposium*, 2007, pp. 981-984.

[4] F. L. Lizzi, M. Astor, T. Liu, C. Deng, D. J. Coleman, and R. H. Silverman, "Ultrasonic spectrum analysis for tissue assays and therapy evaluation," *International Journal of Imaging Systems and Technology*, vol. 8, pp. 3-10, Sept. 1996.

[5] F. L. Lizzi, M. Greenebaum, E. J. Feleppa, and M. Elbaum, "Theoretical framework for spectrum analysis in ultrasonic tissue characterization," *Journal of the Acoustical Society of America*, vol. 73, pp. 1366-1373, April 1983.

[6] M. F. Insana, R. F. Wagner, D. G. Brown, and T. J. Hall, "Describing small-scale structure in random media using pulse-echo ultrasound," *Journal of the Acoustical Society of America*, vol. 87, pp. 179-192, Jan. 1990.

[7] J. Mamou, M. L. Oelze, W. D. O'Brien, Jr., and J. F. Zachary, "Identifying ultrasonic scattering sites from three-dimensional impedance maps," *Journal of the Acoustical Society of America*, vol. 117, pp. 413-423, Jan. 2005.

[8] L. E. Kinsler, A. R. Frey, A. B. Coppens, and J. V. Sanders, *Fundamentals of Acoustics*, 4th ed. New York, NY: John Wiley and Sons, 2000.

[9] J. G. Proakis and D. G. Manolakis, *Digital Signal Processing*. Upper Saddle River, NJ: Pearson Prentice Hall, 2007.

[10] M. F. Insana and T. J. Hall, "Parametric ultrasound imaging from backscatter coefficient measurements: Image formation and interpretation," *Ultrasonic Imaging*, vol. 12, pp. 245-267, 1990.

[11] J. Mamou, M. L. Oelze, W. D. O'Brien, Jr., and J. F. Zachary, "Extended three-dimensional impedance map methods for identifying ultrasonic scattering sites," *Journal of the Acoustical Society of America*, vol. 123, pp. 1195-1208, Feb. 2008.

[12] D. P. Bertsekas, *Nonlinear Programming*, 2nd ed. Belmont, MA: Athena Scientific, 2003.

[13] R. C. Gonzales and R. E. Woods, *Digital Image Processing*, 2nd ed. Upper Saddle River, NJ: Pearson Prentice Hall, 2002.